

## **Formation and evolution of turbulence**

### **in convectively unstable internal solitary waves of depression**

#### **shoaling over gentle slopes in the South China Sea**

Tilemachos Bolioudakis,<sup>a</sup> Theodoros Diamantopoulos,<sup>a</sup> Peter J. Diamessis,<sup>a</sup> Ren-Chieh Lien,<sup>b</sup>  
Kevin G. Lamb,<sup>c</sup> Gustavo Rivera-Rosario,<sup>a</sup> Greg N. Thomsen,<sup>d</sup>

<sup>a</sup> *School of Civil and Environmental Engineering, Cornell University, Ithaca, New York*

<sup>b</sup> *Applied Physics Laboratory, University of Washington, Seattle, Washington*

<sup>c</sup> *Department of Applied Mathematics, University of Waterloo, Waterloo, Canada*

<sup>d</sup> *Wandering Wakhs Research, Austin, Texas*

arXiv:2502.01607v1 [physics.ao-ph] 3 Feb 2025

*Corresponding author:* Tilemachos Bolioudakis, tb424@cornell.edu

**ABSTRACT:** The shoaling of high-amplitude Internal Solitary Waves (ISW) of depression in the South China Sea (SCS), is examined through large-scale parallel turbulence-resolving high-accuracy simulations. A select, near-isobath-normal, bathymetric transect of the gentle SCS's continental slope is employed together with stratification and current profiles obtained by in-situ measurements. Simulations are conducted using a state-of-the-art high-accuracy hybrid Spectral-Element-Method/Fourier three-dimensional non-linear non-hydrostatic flow solver. Three simulations of separate ISWs with initial deep-water amplitudes in the range [136m, 150m] provide a novel wave-tracking capability for a propagation distance of 80km. While key features of the in-situ observed phenomena are accurately reproduced, additional insights into wave evolution are offered, inaccessible through field observations. The interplay between convective versus shear instability as a function of deep-water ISW amplitude, along with the associated turbulence formation and evolution, are explored. Across all three waves, the convective instability develops in a similar fashion. Heavier water entrained from the wave rear plunges into its interior, giving rise to transient, yet distinct, subsurface vortical structures. Ultimately, a gravity current is triggered which horizontally advances through the wave interior and mixes it down to the base of the pycnocline. Although the waveform remains distinctly symmetric, Kelvin-Helmholtz billows result near the well-mixed ISW trough, disturb the wave's trailing edge, and are linked with an active wake with an intensity nonlinearly dependent on deep-water wave amplitude. Finally, the evolution of the kinetic energy associated with finer-scale velocity perturbations to the ISW shows two different growth regimes, each dominated by either convective or shear instability.

## 1. Introduction

Internal solitary waves (ISWs) are ubiquitous oceanic phenomena found on continental slopes and shelves, in submarine canyons, and over oceanic topographic features (e.g. Sandstrom and Elliott 1984; Klymak and Moum 2003; Scotti and Pineda 2004; Carter et al. 2005; Moum et al. 2003, 2007; Shroyer et al. 2011; Lien et al. 2005, 2012, 2014; Zhang and Alford 2015; Cheng et al. 2024). Oceanic ISWs of depression are nonlinear, and non-hydrostatic waves, characterized by a large vertical displacement of the pycnocline. Due to the balance between nonlinear steepening and physical dispersion, ISWs can transport energy and mass over long distances while maintaining their waveform (Jackson et al. 2012). Such waves have also been observed to become unstable as they propagate over varying bathymetry, resulting in mixing and energy dissipation far from their generation site (Lamb et al. 2019). ISWs are on the receiving end of oceanic energy cascade originating from the larger-scale input of the internal tides and winds (Helfrich and Melville 2006; Stastna 2022). Additionally, ISWs are efficient suppliers of nutrients into the upper ocean, as they transport the particulate matter they entrain over long distances towards the continental shelf and exchange it with the surrounding water (Lamb 2002; Lien et al. 2012). Consequently, they affect the heat, salt, nutrient, and mass fluxes between the open ocean and coastal waters, and are therefore crucial for primary production and marine ecology (Sandstrom and Elliott 1984; Moore and Lien 2007).

This study is motivated by field observations in the South China Sea (Lien et al. 2012, 2014) of convectively unstable mode-1 shoaling non-linear internal waves where a subsurface recirculating core distinctly formed. The observations of Chang et al. 2021b confirmed the hypothesis of Lien et al. 2012, 2014 that convective instability of ISWs is a systematically occurring phenomenon in this particular region. Convective instability is generated when the maximum wave-induced velocity exceeds the wave celerity (Lamb 2002), while the subsurface recirculating core can be described as a region with closed streamlines (Aigner et al. 1999), computed in a frame of reference moving with the wave (Lamb 2003; Rivera-Rosario et al. 2020), where the maximum wave-induced horizontal velocity occurs well below the surface. For a subsurface core to form the sign of the pre-existing vorticity of the near-surface background current has to be opposite of that generated by the propagating wave (He et al. 2019). In addition, the size of the convectively unstable region generated is largely determined by the magnitude of the near-surface transverse vorticity,

while the interaction with the gently varying bathymetric slope accelerates the subsurface core formation (Rivera-Rosario et al. 2020, 2022). Numerical studies have shown that, during the onset of convective instability, heavier fluid from the rear of the wave plunges forward on top of lighter fluid as it enters the wave interior, producing an overturning and recirculating pattern. However, this subsurface instability, which is confined to the wave interior, is not abrupt enough to cause a complete wave disintegration, as observed during ISW breaking where the pycnocline intersects the slope (Helfrich 1992; Vlasenko et al. 2006). Instead, the ISW maintains a nearly symmetric waveform as it continues to shoal towards the continental shelf (Lien et al. 2014).

The convectively unstable core is linked to enhanced turbulent mixing and energy dissipation inside the ISW (Lien et al. 2012). In the meantime, the core has also been found to exchange its water mass with its environment through a "leaky" behavior strictly linked with the tail of the wave, with what was inferred to be a trailing turbulent wake (Moum et al. 2003; Lien et al. 2012).

Shear instability and Kelvin–Helmholtz (K–H) billows were first observed with biosonic measurements within the interior of a mode-1 ISW on the Oregon shelf by Moum et al. (2003). The authors report shear instability initiated both at the leading edge and the trough of observed ISWs. Recent observations have suggested that shear instability can also originate in convectively-unstable waves through the resulting mixing of the wave core and weakening the stratification therein, namely at the wave trough (Chang et al. 2021b). Moreover, the accompanying enhancement of the vertical shear is generally found to be stronger along the lower periphery of the wave core, while stronger stratification is located predominantly between the periphery of the wave core and the pycnocline (Carr et al. 2011), a combination that works favorably for shear instability to occur (Chang et al. 2021b). In contrast to Moum et al. (2003), both Chang et al. (2021b); Chang (2021) and Lamb et al. (2019) report K-H billows to mainly emerge near the trough of the wave, where the Richardson number ( $Ri = N^2/S^2$ ;  $N$  and  $S$  are the Brunt-Väisälä frequency and the vertical shear) is less than 1/4. The billows grow while traveling toward the ISW rear along the wave interface until their collapse, a process that can non-trivially modify the observed symmetric waveform.

Clear signatures of shear and convective instabilities within the ISWs have rarely been observed in the ocean due to their intermittency and rapid evolution of such phenomena in conjunction with limited measurement resolution (Chang et al. 2021b). Nonetheless, caution is warranted when attempting to leverage the, otherwise illuminating, insights of various laboratory (e.g. Troy and

Koseff 2005; Carr et al. 2008; Fructus et al. 2009) and numerical studies (e.g. Barad and Fringer 2010; Carr et al. 2011; Lamb and Farmer 2011; Carr et al. 2012; Stastna and Legare 2024) towards interpreting the physics of the large-amplitude ISWs observed in the SCS. The SCS (and other in-situ) waves reside in a different regime of the parameter space than their above laboratory/numerical counterparts which focus on internal wave instability over *steep* slopes ( $> 5\%$ ) and are primarily limited to the laboratory-scale. In some cases, in the context of numerical studies, a wave-fixed frame of reference may be used which precludes the use of variable bathymetry (Lamb et al. 2019).

The tracking of ISW propagation over gentle slopes while capturing the associated instability-driven localized turbulence has not yet been possible in the laboratory or through numerical simulations due to the lack of sufficiently long facilities or computational domain required. Moreover, the range of turbulent scales attainable in the laboratory or through numerical modeling is significantly restricted with respect to the ocean (Lamb et al. 2019).

Simulating the shoaling of ISWs in the SCS while resolving the resulting instabilities and (at least the larger scales of the) highly energetic turbulence in the wave interior, as reported by Lien et al. 2012, 2014; Chang et al. 2021b, poses a state-of-the-art challenge in ocean modeling. To this end, the characteristic lengthscales of interest extend from  $O(100\text{ km})$  propagation distances and transition down to the wavelength ( $O(1\text{ km})$ ) and the scales of the convectively-driven overturn ( $O(100\text{ m})$ ), K-H billows ( $O(10\text{ m})$ ) and finally turbulence ( $O(1\text{ m})$ ).

The spectral-element method (SEM) is optimally suited for the above multiscale problem, as it can adequately capture the wave-scale response to the bathymetry and resulting finer-scale phenomena without the spurious influence of numerical dispersion and dissipation (Diamantopoulos et al. 2022). One can also leverage the SEM's ability to localize resolution within the wave core in the vertical and progressively reduce it in the along-wave direction as the ISW approaches the convective instability location.

This study builds on the previous work of Rivera-Rosario et al. (2020); Diamantopoulos (2021), while using the SEM-based flow-solver of Diamantopoulos et al. (2022), and reports on high-accuracy-resolution and fully nonlinear/non-hydrostatic simulations of ISWs in the SCS bathymetry in both two and three-dimensions. The primary objective of this effort is to computationally investigate the wave-and-finer-scale response of high-amplitude ISWs when shoaling over realistic gentle slopes in the SCS with in-situ-sampled background current/stratification profiles. In particular, the

convective instability and the resulting subsurface recirculating core are examined from not only a structural but also a quantitative standpoint. Additional focus is placed on the resulting turbulence, its spatial distribution within the wave, and its capability to subsequently induce shear instabilities and an energetic wake in the rear of the wave. Three initial waves with different amplitudes are simulated separately to examine the potentially nonlinear dependence of wave evolution and the above finer-scale phenomena to initial deep-water wave amplitude (defined as the maximum isopycnal displacement).

This paper is structured as follows: Section 2 describes the oceanic region of interest and field conditions that dictate the configuration of the computational domain. The governing equations and the numerical method are also reviewed. Section 3 contrasts initially the two versus the three-dimensional simulations and subsequently analyzes and inter-compares the actual turbulence-resolving simulations using both qualitative and quantitative metrics. Finally, section 4 contains the summary and discussion of the overall findings and open questions.

## 2. Method

### *a. Problem geometry*

The broader area of interest is the South China Sea, which is considered a semi-enclosed marginal sea in the western Pacific Ocean and is characterized by a  $> 3$  km deep basin depth that gradually decreases from east to west, tracking the gentle slope up to the continental shelf. Figure 1 (a), shows contours of the bathymetry of the region where the ISWs have been observed by Lien et al. (2012, 2014); Chang et al. (2021a,b) and Chang (2021), along with the ship trajectory during their wave racking in the experiment by Lien et al. (2014) (black dotted line). The black contour lines (Fig.1a) highlight the principal bathymetric changes over the approximate transect ISWs were found to propagate. As shown in Fig. 1, the coordinates of the area extend from  $21.07^\circ$  N,  $118.49^\circ$  E to  $21.07^\circ$  N,  $116.50^\circ$  E. The locations of *shallow* ( $21^\circ$ N,  $117.22^\circ$ E) and *deep* ( $21^\circ$ N,  $117.27^\circ$ E) moorings deployed by Lien et al. (2014) (in the particular paper they were referred to as “surface” and “subsurface” respectively) are also indicated, with the orange and red stars on Fig. 1(a) and with vertical dotted lines on Fig. 1(b). The bathymetric data for Fig. 1(a) are obtained from the General Bathymetric Chart of the Oceans (GEBCO). However, the data actually used in the

bathymetry of the high-resolution simulations reported here are sampled from Lien et al. (2005)'s high-accuracy measurements and denoted via the corresponding black dotted line of Fig. 1 (b).

The total length during the wave tracking measurements of Lien et al. (2014) extended over a distance larger than 200 km. The high-accuracy/resolution numerical simulations reported here follow the approach of Rivera-Rosario et al. (2020, 2022). In particular, the numerically investigated region focuses on the transect between  $21^\circ\text{N}$ ,  $117.8^\circ\text{E}$  and  $21^\circ\text{N}$ ,  $117.0^\circ\text{E}$  (80km in length), including the locations of both moorings and indicated by the solid blue line in both Fig. 1 (a) and (b).

Moreover, the actual coordinates for the simulation have to be adapted to a Cartesian coordinate system, to be consistent with the equations of motion (shown in the next subsection). Thus, a converted form, from latitude–longitude to universal transverse Mercator, is applied. In addition, under the assumption of negligible latitudinal change for the given longitudinal displacement of the transect, the small deviations in the northing direction and the associated bathymetric variations can be safely neglected. At this point, one should note that in the three-dimensional computational coordinate system,  $x$  is taken to represent the east-west direction,  $z$  is the bottom-surface direction, and  $y$  is the transverse (north-south) direction. In the simulation's framework, the  $\hat{i}$  vector points towards the wave propagation direction (westward). Although the unitary vector  $\hat{k}$  points from the bottom to the surface, all the figures presented in this paper use a positive sign on the vertical axis, leaving the "Depth" notation to denote distance below the surface.

### *b. Field conditions*

The aforementioned moorings, equipped with conductivity–temperature–depth sensors (CTD) and acoustic current Doppler profilers (ADCP), recorded data over five successive days (31 May 2011 to 3 June 2011; see Lien et al. 2014 for details), the subsurface recirculating core of a convectively unstable ISW was first observed at this site on June 2nd. Under the constraint that the background current-induced vorticity sign be favorable for the recirculating core to form (see He et al. 2019), the time-averaged water column properties measured before the arrival of the first wave observed on June 2nd are used to set the background conditions in the simulations reported here. In Fig. 2, the time-averaged background horizontal current velocity (a), shear (b), density (c) and squared Brunt-Väisälä frequency  $N^2$  (d) profiles sampled, are shown with black lines.

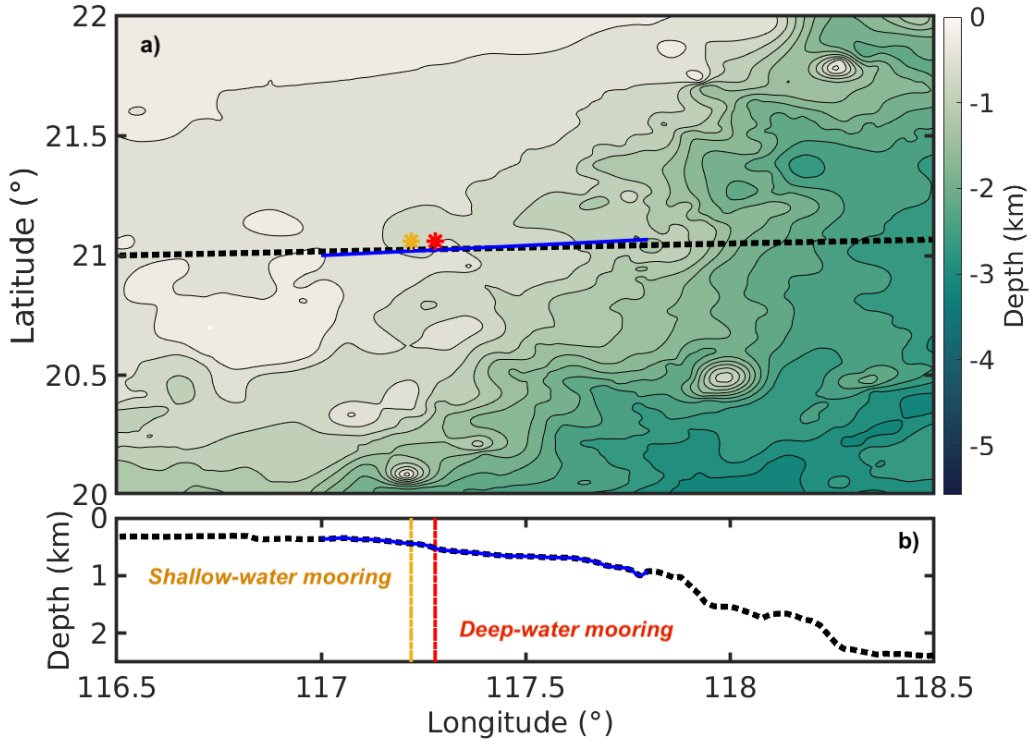


FIG. 1. Bathymetry map of the northern section of the South China Sea (a), in conjunction with the water depth along the transect (black dotted line in b). The black dotted line on (a) the ship trajectory during the wave tracking in Lien et al. (2014). The solid blue line shows the region of this transect that is taken into account in our simulations shown hereafter. Lastly, the *shallow* (orange star) and the *deep* moorings' (red star) locations are indicated, deployed 6km apart and covering the upper continental area. The colormap used is based on Thyng et al. (2016).

Note that, in agreement with Rivera-Rosario et al. (2020), near the surface background velocity is set to be negative (of opposite sign to what is reported in Lien et al. (2014)) because in this study the positive direction is taken to be the westward (see also section 2a). Following Rivera-Rosario et al. (2020), the background horizontal velocity profile in the 10 upper meters of the water column is obtained from linear extrapolation upward, due to the absence of in situ data. The horizontal velocity is gradually set to zero after 300 m of depth, preventing any hydraulic effects associated with the interactions between the bottom fluid layer and the gentle slope. The resulting velocity and shear profiles used in this study are shown as the blue lines in Fig. 2(a) and (b). In addition, all four profiles are strictly one-dimensional, and thus no variation in either horizontal direction



is considered. Moreover, assuming ISWs with propagation speeds comparable to the principal internal tide propagation speed, the background fields are held steady throughout the simulation. Last but not least, the depth where the maximum BV frequency is detected ( $z_0 = -22m$ ), indicates the position of the pycnocline. The resulting value of density at this depth is set as the reference density ( $\rho_0 = 1022.58 \text{ kg} \cdot \text{m}^{-3}$ ).

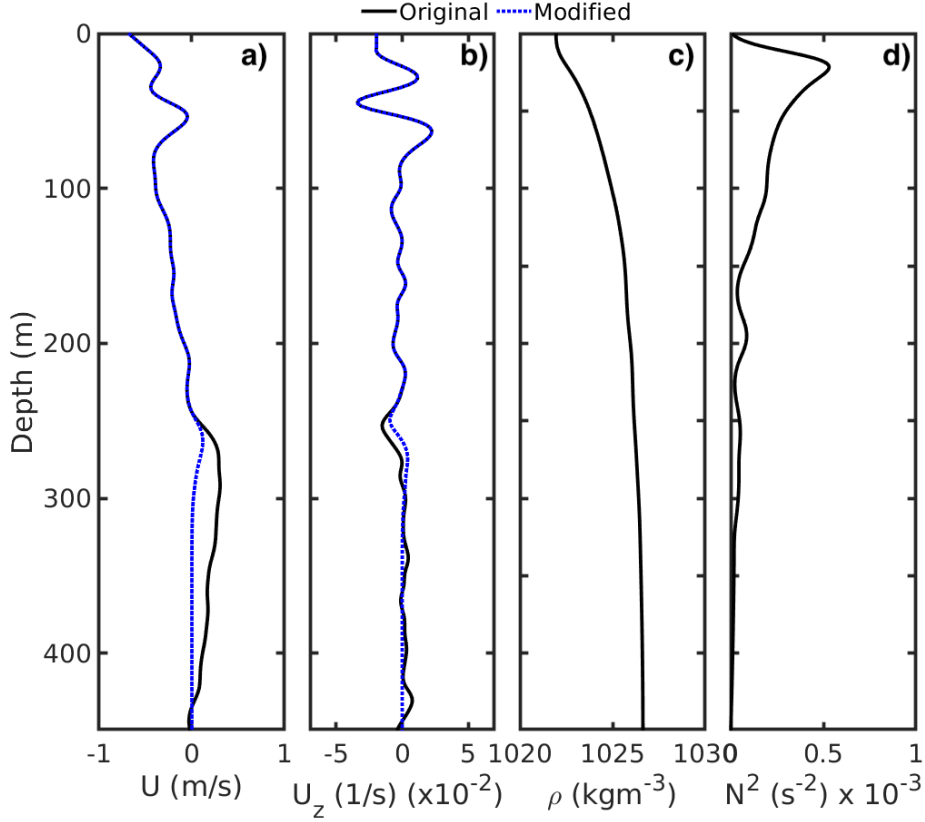


FIG. 2. Time-averaged vertical profiles of the background (a) current, (b) shear, (c) density, and (d) squared Brunt–Väisälä frequency used in this study. The velocity profile shown involves a change in sign, identically to Rivera-Rosario et al. (2020) with respect to that originally sampled and reported by Lien et al. (2014). The blue line shows the modified profiles used as background conditions in this numerical study, to ensure the absence of any potential hydraulic interaction of the background current with the gently varying bathymetry.

### c. Governing equations

In the present study, the mathematical model uses the incompressible Euler equations under the Boussinesq approximation (IEEB),

$$\frac{\partial \mathbf{u}}{\partial t} = -\mathbf{u} \cdot \nabla \mathbf{u} - U \frac{\partial}{\partial x} \mathbf{u} - w \frac{\partial U}{\partial z} \hat{i} - \frac{1}{\rho_0} \nabla p' - \frac{g}{\rho_0} \rho' \hat{k} , \quad (1)$$

$$\frac{\partial \rho'}{\partial t} = -\mathbf{u} \cdot \nabla (\bar{\rho}(z) + \rho') , \quad (2)$$

$$\nabla \cdot \mathbf{u} = 0 , \quad (3)$$

where, any possible effect of planetary rotation is neglected, as the shoaling effects are suggested to dominate over the depth of interest (Lamb and Warn-Varnas 2015). Here  $U(z)$  is a background current oriented along the wave propagation direction; it is assumed to be steady. One effectively solves for the three-dimensional vector  $\mathbf{u}$ , in three-dimensional Cartesian coordinate space where  $\mathbf{x}$  is the vector of position therein, which consists of contributions from the two-dimensional wave-induced field and the subsequent turbulence.

Accordingly, the density field is decomposed into a reference value  $\rho_0$  (value taken from depth where  $N^2$  is maximum), a steady background profile  $\bar{\rho}(z)$  (obtained from the profiles measured in the water column) and a wave/turbulent perturbation  $\rho'$ , such that  $\rho = \rho_0 + \bar{\rho}(z) + \rho'(\mathbf{x}, t)$  with  $\rho_0 \gg \bar{\rho}(z) \gg \rho'(\mathbf{x}, t)$ . The hydrostatic balance between the reference pressure, away from the wave, and the background density has been subtracted from equation (1);  $p'$  represents the corresponding pressure perturbation.

The simulations reported here are inviscid and non-diffusive. Neglecting the viscous and diffusive terms is based on the assumption that the smallest-resolved physical lengthscales are far larger than the Kolmogorov and Batchelor scales. In addition, any potential viscous effects at the bed due to a no-slip boundary condition and the associated turbulent boundary layer, are assumed to negligibly impact the large-scale wave structure and the convective instability and are outside of the scope of this study.

With the exception of the periodic transverse direction, no boundary conditions are enforced in the velocity and density fields due to the inviscid/non-diffusive formulation of the governing equations. The pressure is subject to nonhomogeneous Neumann boundary conditions on the  $x - z$  plane (Karniadakis et al. 1991).

#### *d. Numerical Method*

##### 1) GENERATING THE INITIAL CONDITIONS

The initial two-dimensional ISW is generated identically to Rivera-Rosario et al. (2020). The fully nonlinear Dureuil-Jacotin-Long (DJL) equation (Long 1953; Turkington et al. 1991) is solved using the pseudospectral method of Dunphy et al. (2011) for the observed background conditions (Fig. 2) and prescribed available potential energy value. The resulting isopycnal displacement field  $\eta(x, z)$  is used to construct the associated density  $\rho'$  and velocity ( $u$  &  $w$ ) fields. The wave-representing fields are then interpolated onto the desired computational grid and finally inserted over a deep-water artificial plateau (Fig. 3) to prevent any potential spurious shoaling effects during the initialization.

##### 2) HYBRID NODAL SPECTRAL ELEMENT / FOURIER NUMERICAL METHOD

The numerical tool used in this study is a hybrid Nodal-Spectral-Element/Fourier-Galerkin-Method-based (NSE/FGM) flow solver for the incompressible Navier–Stokes equations, under the Boussinesq approximation in doubly non-periodic deformed domains (Diamantopoulos et al. 2022). For the bathymetry of choice, two-dimensional simulations are conducted over a vertical plane normal to the isobaths. A third, Fourier-discretized, periodic direction may be readily incorporated in the transverse to conduct simulations aimed to resolve turbulence. Note that the bathymetry is one-dimensional (strictly a function of the along-wave direction), and any potential lateral variations in depth are not accounted. In addition, non-hydrostatic effects, a critically important part of shoaling ISW dynamics, are accounted for through a fast hybrid direct/iterative solver for the two-dimensional pressure Poisson equation (PPE) for each transverse Fourier mode based on a three-level Schur-complement approach based decomposition of the grid which is highly parallelizable (Karniadakis and Sherwin 2005; Joshi et al. 2016; Diamantopoulos et al. 2022).

Numerical stability of the SEM solver is enabled explicitly through the application of a  $10^{th}$  and  $15^{th}$  order exponential spectral filter in the non-homogeneous  $x$ - $z$  plane and periodic  $y$ -direction respectively (Diamessis et al. 2005 and Diamantopoulos 2021), equivalent to the use of hyperviscous operators (Boyd 1998; Gottlieb and Hesthaven 2001). Each velocity component and density perturbation are filtered once every time-step after the computation of the non-linear and advective terms respectively (Diamantopoulos et al. 2022), in contrast to Rivera-Rosario et al. (2022).

Additional stabilization is achieved in the  $x - z$  directions via “polynomial dealiasing” (Kirby and Karniadakis 2003), of the non-linear and advective terms (Malm et al. 2013; Diamantopoulos et al. 2022). Lastly, an artificial Rayleigh-type damper, two ISW-width thick, is applied to the left and right boundaries to eliminate any possible reflection from the incoming ISW (Rivera-Rosario et al. 2020).

### *e. Simulation description*

#### 1) INITIALIZATION OF THE SIMULATIONS

The ISW is initialized on the deep-water artificial plateau (Fig. 3) and progressively advances into shallower waters across the entire 80 km-long propagation track. Note, however, that the term “plateau” will hereafter be reserved to refer to the almost uniform-depth bathymetry which begins at the 68<sup>th</sup> km of the transect.

The simulations reported here are actually conducted in an overlapping window framework (see Rivera-Rosario et al. 2022 and Diamantopoulos et al. 2022 for more detail): the computational domain is divided up into sub-regions successively overlapping in the direction of wave propagation. The use of the overlapping window allows one to efficiently simulate the ISW as propagating feature localized, nevertheless, within a particular window.

The maximum number of available grid points, as dictated by the computational resources at hand, is then focused on a single window. Each three-dimensional window’s length extends to approximately 12 wavelengths in the  $x$ -direction (corresponding to almost 12 km), while each overlapping region accounts for 6 wavelengths on average. Per the above approach, the targeted spatial resolution of 1m or less (see section 2e2) is attained, namely on the  $xz$ -plane.

All simulations are initially run in two-dimensional mode. The along-wave spectral element dimension is progressively decreased prior to ISW arrival at the region of convective instability, accordingly reducing the minimum grid-spacing, to ensure optimal resolution of the instability and resultant turbulence (Diamantopoulos 2021). Elements are finer within unstable/turbulent ISW interior and coarser in the less active regions above/below it (Diamantopoulos 2021).

At least three initial wavelengths ( $\approx 3km$ ) prior to the onset of the primary two-dimensional convective instability, the simulation switches to three-dimensional mode by extruding the domain in the periodic transverse direction. To enable a bypass transition to turbulence (Schmid and

Henningson 2001) during the convective instability stage, finite-amplitude velocity and density perturbations are inserted. The remaining wave propagation distance until the onset of convective instability ( $\sim 3 L_w$ ) enables any potentially laterally unstable mode, with a higher growth rate than the primary convective two-dimensional instability, to develop (Winters and Riley 1992; Winters and D’Asaro 1994). Nonetheless, we have found that the primary convective instability in this study has always been strictly two-dimensional.

Specifically, white Gaussian noise with a standard deviation  $\sigma = 10^{-2}$  and maximum amplitude  $A_{noise} = 0.015$  (units are  $m/s$  and  $kg/m^3$  for velocity and density, respectively), is inserted immediately after the transition to three-dimensional mode. Such a perturbation field is inserted in  $y$ -Fourier space over the first seven non-zero modes of only  $u$ ,  $w$ , and  $\rho'$  components. The energy content of any higher transverse Fourier modes builds up naturally through nonlinear interactions and the resulting downscale energy cascade. The initial  $v$  perturbation field is created through continuity, and the IEEB solver’s projection step (Diamantopoulos et al. 2022), similar to Fringer and Street (2003). Finally, the initial perturbations are windowed onto a “masking” function on each  $x$ - $z$  plane to prevent any spurious numerical instabilities at the domain boundaries (Diamantopoulos 2021).

Three production runs were conducted with different initial wave amplitudes ( $\eta_{max}^{init}$  in meters): 136 (*small*), 147 (*baseline*), and 150 (*large*). The location of transition into a three-dimensional simulation for each wave is contingent on the critical depth of onset of the dominant two-dimensional convective instability, itself set by both the wave amplitude and the bathymetric changes, effectively occurring earlier along the propagation track with increasing initial wave amplitude (Rivera-Rosario et al. 2020).

For all three simulations, the analysis reported in section 3 is based on explicitly postprocessing large three-dimensional simulation output files. This large file size (24 Gb per file) imposes a practical constraint on the frequency at which these files are outputted during the simulation. As such, files are outputted every [1224, 2913] time steps (depending on the adaptively set time step value; see section 2e2) which corresponds to an output rate in the range of [270, 339] *sec* in simulation time units and an along-propagation-track spacing of [367, 607] *m*. This relatively coarse output rate limits the temporal resolution with which one can examine, in a postprocessing sense, the evolution of the K-H billows generated at the ISW-trough (section 3e4).

## 2) CONSTRUCTION OF THE COMPUTATIONAL DOMAIN

Figure 3 shows potential density ( $\sigma = \rho - 1000$ ) contours in the full computational domain, with the initial ISW in deeper water. The bathymetric transect matches the one reported in Fig. 1b (blue line). The locations of the original moorings deployed by Lien et al. (2012) are also shown. Furthermore, the additional 20km uniform-depth region is denoted before the beginning of the transect (note the negative sign in figure’s 3 horizontal axis). During the transition to the three-dimensional stage, the computational domain is extruded in the  $y$ -direction with a width of  $L_y = 50m$ . Per the rationale outlined in Rivera-Rosario et al. (2022), the particular choice of the lateral domain width accommodates one wavelength of the fastest-growing transverse instability mode of the dominant two-dimensional convective instability (Diamantopoulos et al. 2022).

Each three-dimensional overlapping window contains  $[768 \times 60]$  spectral elements of polynomial order  $p = 7$  on the  $x$ - $z$  plane, which amounts to a total of 290 million grid points per window. Per the flexible reduction in element size in both directions described in section 1 and the non-uniform spacing of the Gauss-Legendre-Lobato grid points in each element (Canuto et al. 2007), the highest resolution attained corresponds to grid spacings  $\Delta x_{min} = 1.03m$  in the horizontal and  $\Delta z_{min} = 0.21m$  in the vertical inside the wave, where the vertical elements are clustered. In the transverse, a Fourier-periodic grid of 128 points is employed yielding a resolution of  $\Delta y = 0.39m$ . In conclusion, this study has markedly higher resolution in all three directions as compared to Rivera-Rosario et al. (2022).

The time-discretization scheme is based on Karniadakis et al. (1991) and further explained in Diamantopoulos et al. (2022). The time step,  $\Delta t$ , size is adaptively chosen during each simulation so as to respect the Courant–Friedrichs–Lewy constraints in all three directions. Soon after the onset of convective instability,  $\Delta t$  is consistently reduced and remains near-constant, however, between 0.1 and 0.2s across all runs.

## 3) COMPUTATIONAL RESOURCES

The massively parallel three-dimensional shoaling ISW turbulence-resolving simulations were conducted on the NSF ACCESS’s allocated HPC systems (Townes et al. 2014 and Boerner et al. 2023). For each run, the parallel execution of the flow solver on each computational window

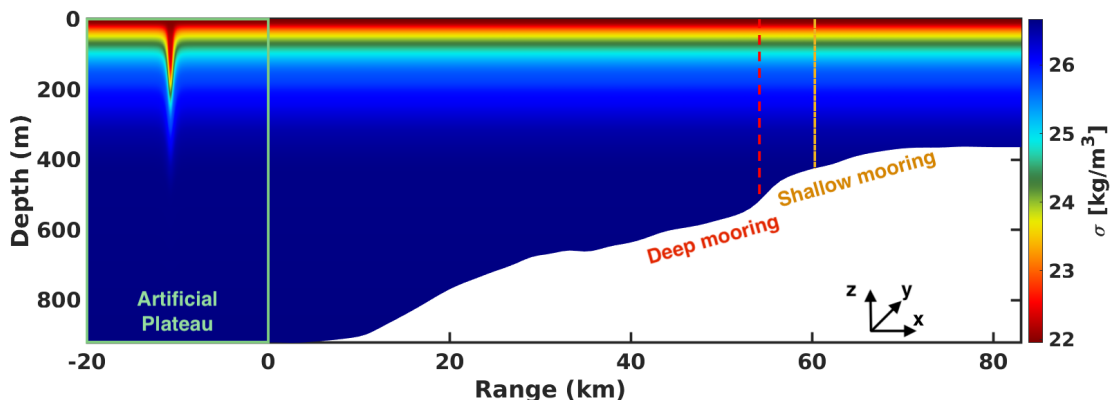


FIG. 3. Full computational domain with potential density contours and initial ISW. Dashed lines indicate the locations of the *shallow* and *deep* moorings respectively, as deployed in the SCS by Lien et al. (2014).

used 6144 cores evenly across 128 nodes on Stampede2 at the Texas Advanced Computing Center (TACC). The wall-clock time for each simulation was 12 days.

### 3. Results

#### *a. Baseline wave evolution*

##### 1) SIMULATION COMPARISON IN TWO AND THREE DIMENSIONS

So far, in the published literature, any computational studies of the shoaling of ISWs over gentle slopes and long domains have largely relied on two-dimensional simulations (Lamb and Warn-Varnas 2015; Rivera-Rosario et al. 2020). Although no results are explicitly shown, in this section we summarize the main similarities and differences between two-dimensional simulations and their turbulence-resolving counterparts in three-dimensions (initiated from the onset of convective instability), as restricted to the *baseline* wave ( $A = 143m$ ) per the comparison already offered in (Diamantopoulos 2021) and (Rivera-Rosario et al. 2022).

Per the calculation approaches outlined in section 3b1, in terms of the evolution of the maximum wave-induced horizontal velocity,  $u_{max}$ , relative to the ISW propagation speed,  $C$ , the onset of the convective instability as denoted by  $u_{max} > C$ ; see intro, occurs at almost the same location for the two and three-dimensional runs, as emphasized in Diamantopoulos (2021). As such, satisfaction of the particular instability criterion is negligibly affected by any early-time finer-scale turbulent motions. In a similar vein, a comparison (not shown in this paper) of the amplitude  $A$  (defined as

the maximum ISW-induced vertical isopycnal displacement  $\eta_{max}$ ) and wavelength  $L_w$ , calculated according to Koop and Butler (1981) and Rivera-Rosario et al. (2022) as,

$$L_w = \frac{1}{A} \int_{-\infty}^{\infty} \eta_{max}(x) dx , \quad (4)$$

for the two-versus-three-dimensional runs reveals nearly identical behaviour as a function of the downstream propagation, corroborating the findings of the lower-resolution simulations of Rivera-Rosario et al. (2022). In conclusion, any three-dimensional effect does not affect dramatically the primary length and velocity scales of the ISW over the entire evolution.

However, as demonstrated in Diamantopoulos (2021), a focused examination of the wave core structure reveals differences in the evolution of the structure of convective instability between simulations in two and three dimensions. The wave interior (hereafter, also referred to as the wave core) is also significantly more mixed, largely due to the larger-scale turbulence captured by the three-dimensional runs (figures 6 and 12). Most importantly, to this end, shear instability occurs only in turbulence-resolving simulations.

Note that a separate two-dimensional run for the baseline wave was performed with the perturbation insertion approach outlined in Section 2e 1. A rapid decay of the perturbations took place with no impact on the longer-development of the ISW core structure.

## 2) FLOW STRUCTURE OF CONVECTIVELY UNSTABLE WAVE EVOLUTION (BASELINE WAVE)

Figure 4 shows the flow structure of the baseline ISW's core at three locations along the transect where convective instability dominates, by visualizing the potential density field through three-dimensional isosurfaces (left) and contour plots sampled on the transverse midplane (right). The reader is recommended to consult the supplementary animations for a more dynamically evolving perspective on the evolution of convective instability. The range of isopycnal surfaces and *contour lines* in Fig. 4 (and Fig. 6) is intentionally chosen such that its lower and higher bounds correspond to two specific isosurfaces in Fig. 4. The first one, drawn in red, effectively illustrates the convective instability onset in the form of the first isopycnal that plunges into the ISW's interior. The second one, drawn in grey, is associated with the peak of the background Brunt–Väisälä frequency in Fig. 2(d) and is an indicator of the pycnocline for the particular background stratification. The former



isosurface also serves as an approximate indicator of the leading edge and top interface of the horizontally advancing gravity current discussed below (see also figures 6 and 12).

The initial stage of ISW convective instability is manifested through the steepening of the lightest visualized isosurface (isosurface and isocontour drawn in red in Fig. 4), which is accompanied by lateral finer-structure development at 53 km. As the wave shoals, heavier isopycnals plunge into its interior. The relative contribution of advection and buoyancy in this process of entraining fluid into the ISW interior remains unclear.

The entrainment of heavier water into the inner wave region (curled cyan and purple iso-contour lines) is even more visible at 56.8 km in Fig. 4. As this entrainment process continues, a sufficient amount of heavier water accumulates inside the wave such that a horizontally-advancing gravity current develops (see supplementary animations). At the *shallow* mooring location (Fig. 4 at 60.2 km), all detached isopycnals have overturned vertically and laterally due to the turbulence associated with the convective plunging and the above gravity current. The gravity current, whose leading edge is denoted by the red isopycnal surface/contour, advances towards the ISW trough and, at later times, past it (see supplementary animations). As the ISW propagates up the plateau, and gravity current turbulence continues to homogenize the entrapped fluid, the ISW maintains the convectively unstable condition of ( $u_{max}/C > 1$ ). Determining quantitatively if the red isopycnal acts like a barrier between the ISW core and the shallower near-surface water or if there is any (and how much) turbulent entrainment across this interface requires further investigation, and is deferred to future study.

The subtle growth in the vertical displacement of the dividing (grey) isopycnal in Fig. 4, as the wave moves into shallower waters (53-60km), indicates a growth in wave amplitude which is consistent with the evolution reported in Rivera-Rosario et al. (2022). At the same time, the waveform remains remarkably symmetric as indicated by the along-wave structure of the same isopycnal. Any steepening effect in the wave rear occurs for lighter isopycnals, internal to the wave, e.g. the red-colored one in Fig. 4. This preservation of the structural integrity of the wave, in the presence of shallow/near-surface pycnocline, is in direct contrast to the simulations of Vlasenko et al. (2005) where the pycnocline intersects the bathymetry and the unstable shoaling wave breaks and terminally disintegrates.

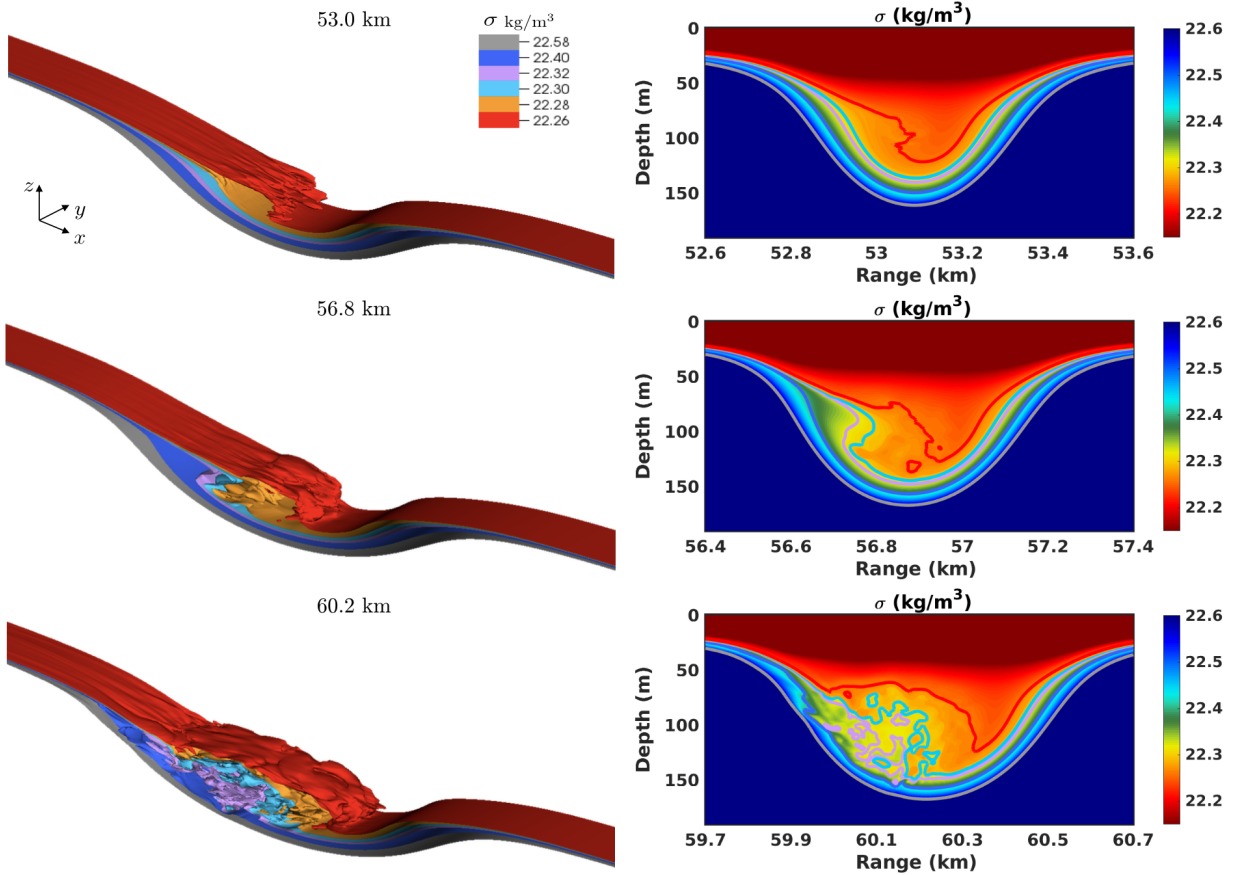


FIG. 4. Evolution of three-dimensional convective instability in the baseline ISW ( $A_{init} = 143m$ ), shown via potential density  $\sigma$  contours. **Left:** Three-dimensional  $\sigma$  isosurfaces at 6 distinct values. **Right:** Mid-plane ( $y = 25$  m) contours at the same downstream location, overlapped with contour lines; line colors and values correspond to the  $\sigma$  isosurfaces of the same color in the left panels. Colorbar values are saturated accordingly to emphasize the convective instability and the entrainment and forward-plunging of fluid. The range of isopycnal surfaces and *contour lines* in Fig. 4 is intentionally chosen such that its lower and higher bounds correspond to the first isosurface to convectively destabilize and to the peak in the background Brunt–Väisälä frequency in Fig. 2(d). A more dynamically evolving view of the convective instability may be found in the supplementary animations and in Diamantopoulos (2021).

Over the same part of the transect, the wave appears to visibly broaden along with the above increase in amplitude. This finding appears to be consistent with the observations of Duda et al. (2004) and predictions of strongly nonlinear theory (Helfrich and Melville 2006; Stastna and Lamb

2002, 2008). Somewhat paradoxically, calculation of ISW wavelength using Eq. (4) shows that this quantity is reduced along the transect, in agreement with Rivera-Rosario et al. (2022).

*b. Three-dimensional runs at different wave amplitudes*

1) CONVECTIVE INSTABILITY DEVELOPMENT

The convective instability develops in a similar fashion across all three simulated waves. Figure 5 shows the maximum value of the transverse-averaged horizontal wave-induced velocity field,  $u_{max}^{<y>}$ , as compared to the associated propagation speed,  $C$ , for each wave. At the deeper part of the transect ( $< 54$  km), larger waves show higher propagation speed (Stastna 2022). Nevertheless, all three simulated ISWs follow a common trend where they decelerate as they propagate over the slope region. The corresponding  $u_{max}^{<y>}$  also monotonically decreases, albeit at a slower rate, and overtakes  $C$ . The critical depth for the onset of the convective instability ( $u_{max}^{<y>} > C$ ) is clearly wave-amplitude dependent, as it occurs earlier along the transect for larger waves in agreement with Lamb (2002) and Rivera-Rosario et al. (2020). The convectively unstable conditions ( $u_{max}^{<y>} > C$ ) persist for the rest of the simulated ISW propagation, with the ratio  $u_{max}^{<y>}/C$  increasing soon before the waves arrive at the steepest slope region closer to the *shallow* mooring (58 – 60 km). Soon thereafter, all ISWs show a local maximum in their  $u_{max}^{<y>}$  which occurs earlier with increasing wave amplitude. Further along the transect,  $u_{max}^{<y>}$  tend to be larger for higher-amplitude waves. However, all propagation speed curves appear to be almost uniform and finally collapse on the plateau at approximately 65 km and onward.

In regards to the *large* wave, marginal convective instability (a persistent state of  $u_{max} \approx C$ ; Chang et al. 2021a) is potentially present per the proximity between the propagation speed and maximum current velocity curves' between 32 to 42 km of the transect. Actually, during its propagation at 32 km, the *large* ISW undergoes an early weak convective instability event: isopycnals initially detach from the rear but then return to their original position, until the subsequent, more powerful, isopycnal plunge takes place as linked to the dominant instability developing at 45 km (see supplementary animations).

Figure 6 shows mid-plane potential density contours zoomed in each wave's core region for the three cases (wave amplitude increasing from top to bottom). Snapshots are shown approximately at 58 km on the left panels, where the steepest slope lies, and at 68 km on the right panels where the

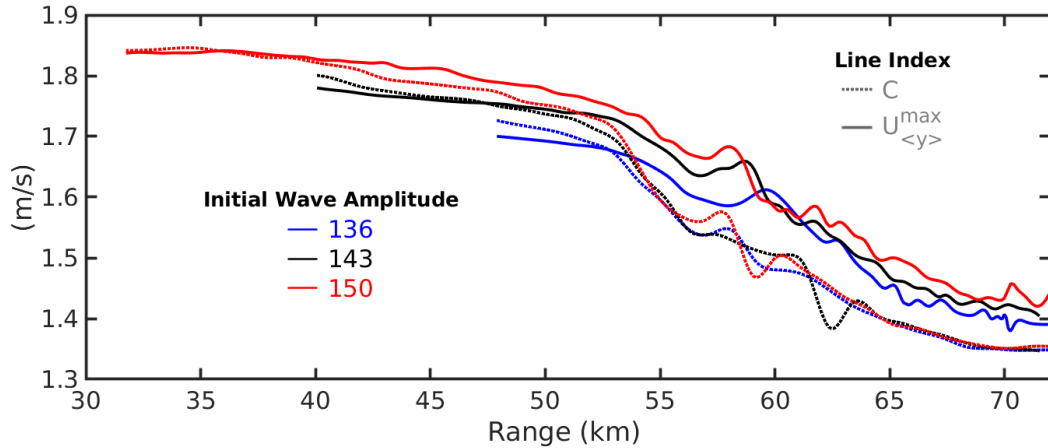


FIG. 5. Maximum horizontal wave-induced velocity  $u_{max}^{<y>}$  (solid lines) and propagation speed  $C$  (dotted lines) for all 3 simulations as a function of the along-wave propagation distance. For each ISW, the corresponding curves begin at the location of initialization of the respective three-dimensional simulation (see Section 2e1). Any indication of the potential for marginal convective instability is restricted to the *large* wave at the earlier stages of the wave evolution (32–42 km).

simulated waves approach the almost-uniform-depth plateau. The ISWs appear to be broader and flatter with increasing amplitude, as also suggested by Lamb (2002); Stastna and Lamb (2002). In the left panels, all ISWs are still in the initial forward plunging stage (see also Fig. 4). Yet, the larger the wave, the earlier the convective instability occurs; more cold water fills the wave’s interior. On the right panels, entrainment from the wave rear and mixing are more clearly visible, both effects being more vigorous for higher amplitude waves. Note that, at this stage, the well-mixed region established by the gravity current in the wave core (see Section 3b 2) has further advanced towards the ISW’s front edge; heavier water mass visibly occupies a greater volume of the ISW core for larger ISWs. This process continues until the end of the simulations, by which point the rear of the wave has been consistently more mixed with colder water with increasing ISW amplitude (see supplementary animations).

## 2) BACKGROUND RECIRCULATION

Streamline visualization is used to investigate the potential for a two-dimensional background subsurface recirculation (see section 1) to form inside the turbulent core of the simulated convectively unstable ISWs, per the equivalent observations of the Lien et al. (2012). Figure 7 shows

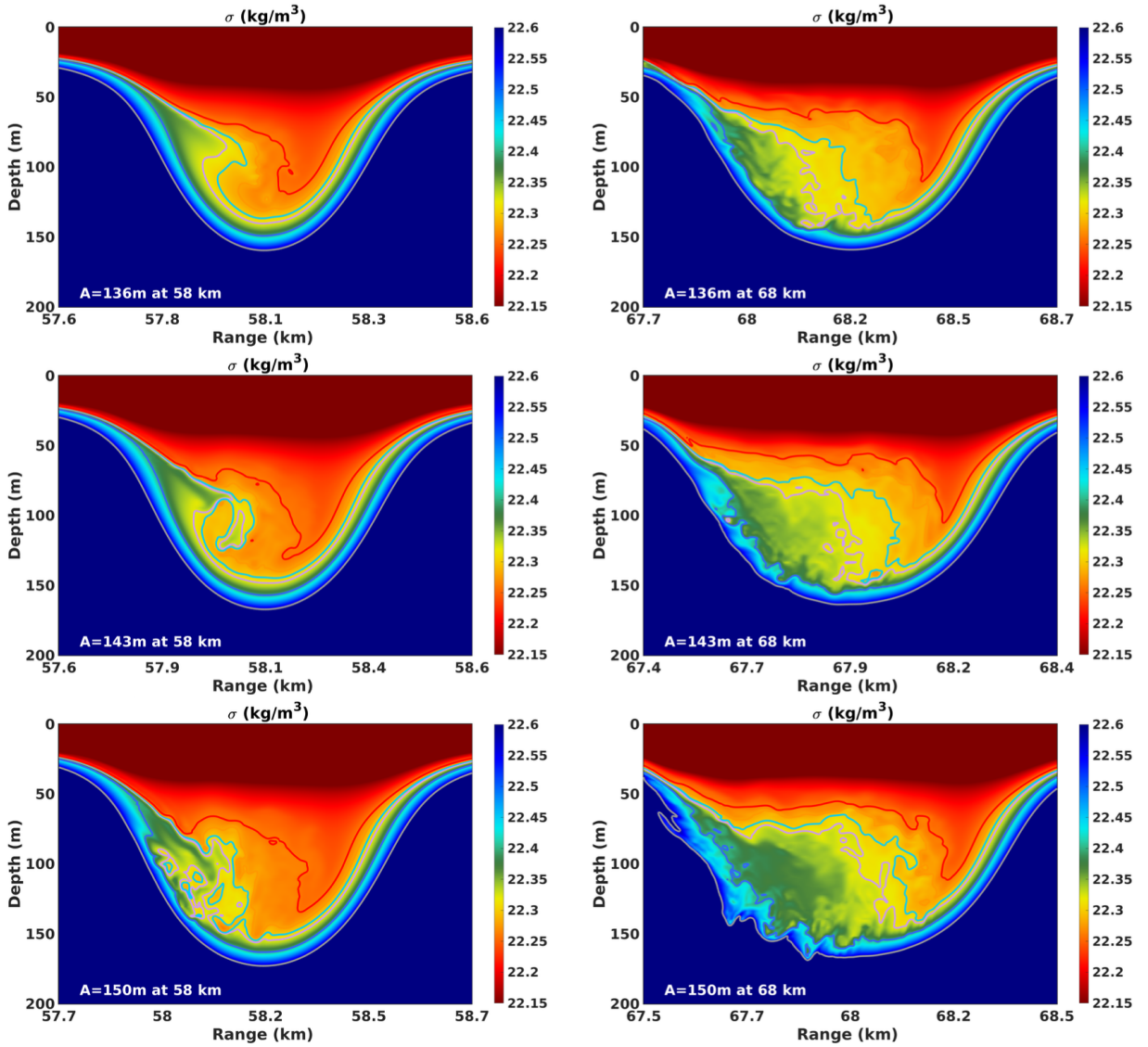


FIG. 6. Mid-plane ( $y = 25$  m) snapshots of the simulated waves captured during the convective instability and its subsequent evolution. **Left:** 58 km & **Right:** 68 km. **Top:** A136, **Middle:** A143, **Bottom:** A150. The flooded potential density contours are shown, overlapped with the same 6  $\sigma$  contour lines of Fig. 4.

streamlines produced by the transverse-averaged velocity field, overlaid on potential density contours. The panels show a distinct background *subsurface* recirculating flow with closed streamlines for all ISWs respectively, sampled at the location of Lien et al. (2012) in-situ observations (*deep* mooring). This primary subsurface recirculation (located in the trough of each wave) is found to occur earlier along the transect with increasing wave amplitude (not shown), and is associated

with the ISW arriving at a critical depth where the convective instability condition,  $u_{max} = C$ , is satisfied. Moreover, the streamline structure of Fig. 7 is similar to the two-dimensional simulations of Rivera-Rosario et al. (2020). However, in that study, the closed-streamline formation is delayed and is not observed, for the wave equivalent to our baseline case, until the wave arrives at the *shallow* mooring location.

In the simulated *large* ISW, a smaller-scale secondary closed-streamline recirculating region develops, associated with the plunging isopycnals in Fig. 6 (*large* ISW at 58km) and baroclinic vorticity generation therein. Consequently, a pair of counter-rotating vortices has been established, in agreement with the observations of Lien et al. (2012). In analogy with the time of emergence of the primary subsurface recirculation, the formation of this secondary vortex structure is delayed with decreasing wave amplitude. As the ISWs advance to shallower water, the two aforementioned counter-rotating vortices interact and move around the rear of the wave. Further downstream, smaller-scale vortical motions develop inside the wave core as the inner region of the ISWs transitions to a less organized state.

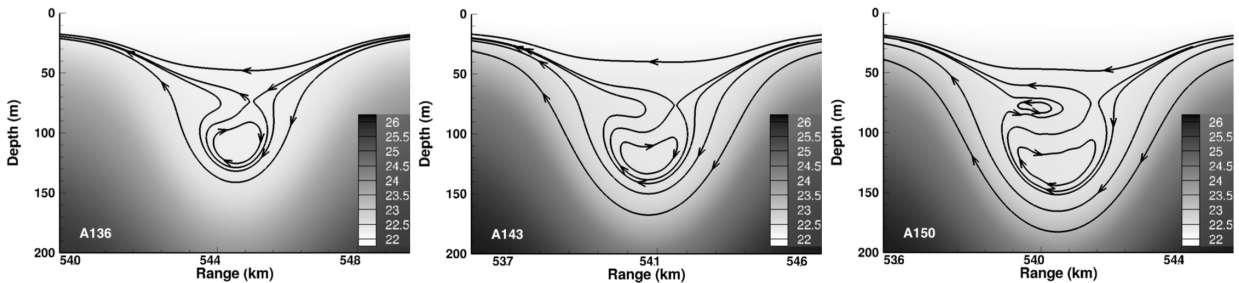


FIG. 7. Velocity streamlines overlaid on potential density contours  $\sigma$ . The arrows on each streamline indicate the direction of the flow. Both potential density values and flow direction correspond to the  $y$ -averaged field computed in a wave-attached frame of reference. The panels compare the three simulated waves at the *deep* mooring location, with increasing amplitude from left to right. A distinct large region with closed streamlines is located in the center of the wave core for all three ISWs, while a second one smaller in size is formed at the *large* wave, creating a pair of counter-rotating vortices. The choice of colormap differs from the one used in previous figures to better highlight the streamlines.

### 3) RICHARDSON NUMBER

The Richardson number ( $Ri = N^2/S^2$ ) may be used as a diagnostic for shear instability in the simulated ISWs (see section 1). Here, the background stratification ( $N$ ) and shear ( $S$ ) are computed using the vertical gradients of the y-averaged fields of density and u-velocity. The critical value for shear instabilities to occur is well-known to be  $Ri_c^p = 0.25$  for parallel stratified shear flows (Smyth and Carpenter 2019). For the finite-length curved stratified shear layer within the ISWs, the adapted criterion of  $Ri_c^c = 0.1$  has been proposed (Fructus et al. 2009; Barad and Fringer 2010; Carr et al. 2011; Chang et al. 2021b; Passaggia et al. 2018; Xu et al. 2019). The alternative criterion of  $L_x/L_w$  ( $L_x$  and  $L_w$  are the length scale of the region with  $Ri < 0.25$  and the ISW wavelength) Fructus et al. (2009); Carr et al. (2011) is not examined in the present study due to the absence of a spatially-coherent-enough band of subcritical Richardson numbers needed to extract  $L_x$  (see Fig. 8).

In Fig. 8, the distribution of the computed  $Ri$  number is shown for all three waves, for two locations on the transect: at the *shallow* mooring (top panel) and at the plateau (bottom panel). The colorbar limit is set to  $[0, Ri_c^p]$  to emphasize the potential for shear instability in a stably stratified background. Inside each simulated ISW core, yellow-to-red colored contours, corresponding to  $Ri \leq 0.1$  criterion are found to extend from the ISW trough to its rear and are weakly offset above the pycnocline (black contour line). These regions of subcritical  $Ri$  have formed due to the mixing and associated weakening of the local stratification produced by the convective instability, and its subsequent evolution, as discussed in Sections 3a2 and 3b1.

The top panels of Fig. 8 display scattered yellow and red patches, while in the bottom panels (sampled at the plateau), a thin yet distinct layer exhibits a higher density of yellow-to-red regions which extend more contiguously over a larger region of the wave. This layer is longer and thicker and has enhanced spatial coherence with increasing ISW amplitude.

Lastly, the robust yellow/red band displayed at the surface region (upper 20 m) is formed due to the background current shear and is not examined in this study. The lack of an inflection point in the near-surface background velocity profile precludes the formation of shear instability therein. Moreover, the absence of any inserted perturbations during three-dimensional initialization within this narrow near-surface layer (section 2e1) and the non-trivial vertical offset of the subsurface

phenomena of interest do not allow for any shear-driven turbulent production within it (Jacobitz et al. 1997).

#### 4) SHEAR INSTABILITY

In situ observations of Moum et al. (2003) in ISWs at the Oregon shelf report 10m-high K-H billows. Subsequent numerical investigations examined the occurrence of shear instability in two-dimensional simulations of ISWs, both in uniform-depth water (Barad and Fringer 2010) and shoaling bathymetry (Lamb and Farmer 2011), reporting a K-H billow thickness of 10m and 5m respectively; the former study also involved a focused study of three-dimensional effects in billow development. In the SCS, the observations of Lien et al. (2014) suggest the existence of shear instabilities, per the measurement of values of Richardson number,  $Ri < 0.11$ . On the continental shelf of the same region, Chang et al. (2021b) actually recorded shear-instability-driven roll-up thermal patterns with vertical scale varying from 15m to 30m in ISWs.

Figure 9 shows potential density contours which demonstrate the earlier occurrences of shear-instability-induced roll-up patterns for all three simulated ISWs at the vicinity of the *shallow* mooring (60 km). With the exception of a very distinct K-H billow in the *baseline* wave, the remaining roll-up patterns in all waves are not shown to fully overturn, at least yet. Whether overturning has not taken place yet, because the shear instability is still developing or it lacks in kinetic energy to overcome the local stratification, requires further investigation. To this end, a higher postprocessing file output rate than the one reported in section 2e1 would be highly advantageous. The less contiguous spatial distribution of subcritical values of the local Richardson number along the ISW trough at this location (yellow-to-red band at the top panels of Fig. 8) would also need to be taken into account. Even without full overturns, evidence of K-H-like patterns that are still shown to form could potentially support Chang (2021), who suggests that K-H billows could potentially occur for ISWs with measured values of  $0.1 < Ri < 0.25$ , and thus concluding if the  $Ri_c^c$  criterion is too restrictive needs further investigation. Similarly, whether the roll-up patterns' puffy structure implies a Holmboe instability, particularly of the Asymmetric type, (Carpenter et al. 2007; Carr et al. 2017; Salehipour et al. 2016, 2018; Olsthoorn et al. 2023) is deferred to future study.



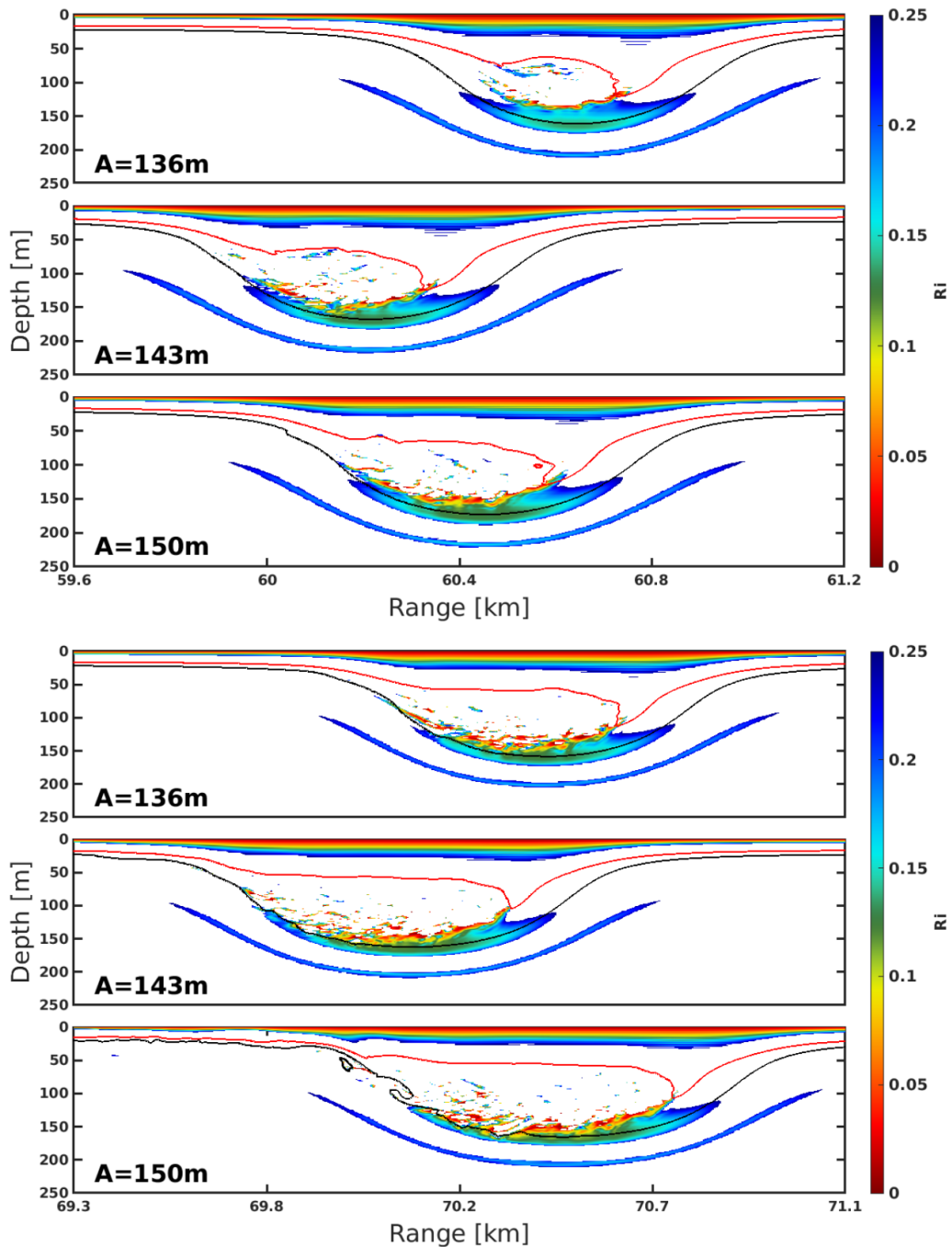


FIG. 8. Transverse-averaged Richardson number contours for all waves at two locations of the transect, at 60 and 70 km respectively. Values only in the range of  $[0, 0.25]$  are plotted, conditions which are considered favorable for shear instability. The red and black contour lines correspond to those in red and grey in figures 4 and 6 and are used to delineate the subsurface recirculating core and the ISW waveform.

Note that Rivera-Rosario et al. (2022) did not observe any clear pattern of shear instability due to limited resolution. In agreement with Chang et al. (2021b), shear-instability-driven overturning features of Fig. 9 have a maximum vertical extent of 20 – 30m in all three waves, as calculated according to Carr et al. (2017). Inspection of transverse-averaged density and along-wave-velocity profiles sampled at the centerline of the wave trough (not shown), show a 100m thick shear layer associated with the ISW signature, equivalent to the measurements of Lien et al. (2014). However, the K-H-billows of Fig. 9 are linked directly with the upper part of this shear layer, where the lower  $Ri$  number region is also found (between 100 and 140m meters, Fig. 8). Lastly, at this stage and across all waves, the K-H-like roll-up patterns are correlated with sufficiently low local  $Ri$  values. Moreover, they are observed to be localized in the transverse direction (not shown) suggesting a potential similarity with the work of Smyth (2004) the exploration of which is, nonetheless, outside of the scope of this study.

At later times, as the ISW is propagating over the plateau, K-H billows with a complete overturn are observed in all simulated waves. For the *small* and *baseline* waves, as shown in the supplementary animations, intermittent pulses of fully-overturned K-H billows are released towards the ISW tails. With the exception of a couple of isolated events, these particular billows mainly form on lighter isopycnals ( $\sigma = 22.3 - 22.4 \text{ kg/m}^3$ ) than the pycnocline, similar to those delineated in Fig. 9. Their height is not significantly greater than what is reported for the events in Fig. 9.

The most dramatic K-H billows occur for the *large* ISW which consistently pulses such features towards its rear. Two such successive events, in the trailing edge of the *large* ISW, are shown in the instantaneous two-dimensional potential density contours on the lateral transect of Fig. 10a. The particular billows, fully overturning, extend to approximately 50m in the vertical which is significantly taller than the events shown in Fig. 9.

An exploded view of the region outlined by the white box in 10a, shows three-dimensional isosurfaces of potential density in Fig. 10b with the two distinct roll-ups corresponding to the two K-H billows discussed above. Finer-scale lateral distortions of the isosurfaces are visible, representative of billow three-dimensionalization (Barad and Fringer 2010), and are typically associated with 4-to-6 rib-like structures with vorticity along the billow periphery (not shown here).

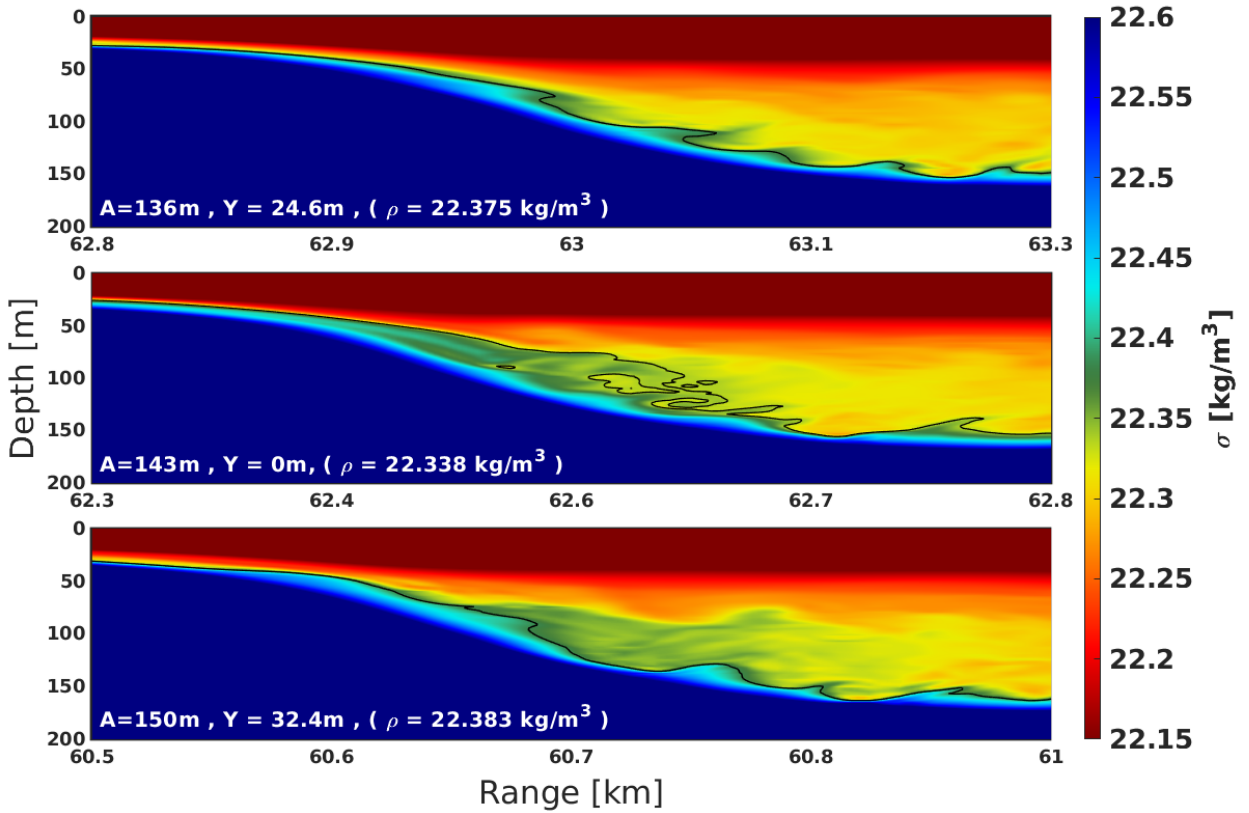


FIG. 9. Shear-induced roll-up patterns in the potential density field within the ISW rear, captured within all three waves at approximately 60 km along the transect. The associated  $x$  coordinate of the wave trough, the  $y$ -location of the selected stream-depth transect, and the reference density (black) contour line value ( $\rho$ ) for each wave have been chosen optimally to best illustrate the roll-up patterns.

The apparent non-negligible transverse coherence of the two billows under consideration is further supported by visualizations of the corresponding spanwise-averaged  $y$ -vorticity field (Fig. 10c). The available resolution, combined with a spectral filter in the transverse direction (Diamessis and Redekopp 2006) are likely preventing further breakdown of the billow into turbulence at this stage of their evolution.

However, consistent with the absence of any overturning of the black isopycnal line on the rear shoulder of the wave or further behind it (Fig. 10a), no other coherent patch of red vorticity lies ahead of these two billows along the shallowest, positive-signed, layer of  $y$ -vorticity in Fig. 10c. The three-layer vorticity structure is a direct imprint of the triple shear layer in the background current profile in the depth range of  $[20, 80]m$  (Fig. 2). At the rear ISW shoulder, one instead

observes a finer-grained feature of red vorticity apparently linked to the breakdown of an earlier billow ascending from the wave trough. A higher postprocessing file output rate (section 2e1) is needed to ascertain such a statement on billow evolution. Per the earlier observation on the additional resolution required for any transverse instabilities to transition into turbulence, this particular billow breakdown is most likely due to its gravitational collapse Smyth and Moum (2000).

Note that any billow-like features, in the form of  $y$ -vorticity roll-ups, behind the wave are actually observed in the middle, negative-signed, of the three  $y$ -vorticity layers. These counter-clockwise-rotating billows appear to be produced by the visibly steep roll-up of the negative  $y$ -vorticity layer by the clockwise-rotating billows generated at the wave trough prior to their breakdown (fig. 10c). Finally, a weak negative  $y$ -vorticity pattern radiating towards the underlying weakly stratified layer is visible in the wave's wake; its investigation is deferred to future studies.

When compared to the in-situ observed billows of Chang et al. (2021b), the numerically simulated ones in Fig. 10 are almost double in size. However, ISWs observed by Chang and coworkers were at least 25m smaller in amplitude than our *large* simulated wave, which could partially explain this discrepancy in billow height. An additional factor behind this discrepancy may be the incomplete three-dimensional evolution of the simulated billows discussed above.

In agreement with a number of past studies (Carr et al. 2011; Barad and Fringer 2010; Lamb and Farmer 2011; Chang et al. 2021b), K-H-like billows are found here to strictly form near the trough of the ISW. A subset of in-situ (Moum et al. 2003; Huang et al. 2022) and laboratory (Carr et al. 2008) studies of similar, but not identical waves and configurations, report billows originating not just at the trough but also the leading edge of the wave. The work of Carr et al. (2008) considered an ISW with a *surface*-attached recirculating core which would likely mix more efficiently the leading of the ISW as contrasted to the subsurface core reported here which mixes the wave trough and rear.

## 5) WAKE ON THE PLATEAU

High-amplitude ISWs have been observed to develop an actively turbulent wake throughout their trailing edge (Moum et al. 2003). Lien et al. (2012, 2014) observed an isopycnal salinity anomaly indicating a wake of mixed water, originating from the mixed ISW core. More recently, Lucas

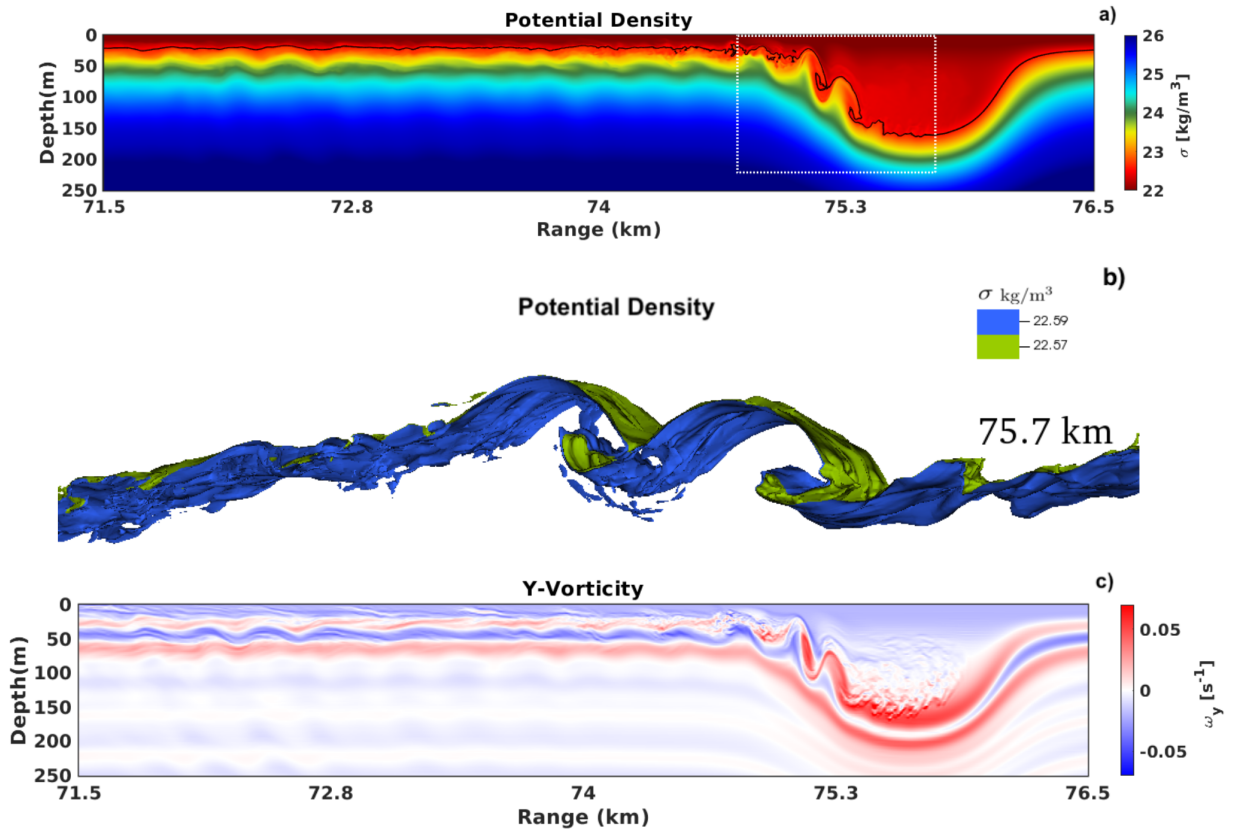


FIG. 10. Instantaneous snapshots of large K-H-billows forming in the *large* ISW rear captured on the plateau at a wave trough location of 76 km: two-dimensional transect of potential density contours (a) and three-dimensional isosurfaces (b). The three-dimensional snapshot (b) is sampled over the white-outlined region of (a) and includes two  $\sigma$  isosurfaces (displayed as black isopycnals in a), weakly separated in magnitude. The axes of b) have been rotated to facilitate a point of view that best highlights the billow. Transverse-averaged y-vorticity contours are also shown in (c). The presence of two distinct, robust vortical structures indicates billow coherence in the transverse.

and Pinkel (2022) examined wakes in ISWs of elevation proposed to be produced by transverse instabilities in the wave interior.

The wakes that develop over the plateau for all simulated ISWs are shown in Fig. 11a, by visualizing potential density contours on the stream-depth mid-plane. The field-of-view consists of a 2.5 km-long window which extends behind each wave's trough. An initial inspection of Fig. 11a) suggests that a distinct wake forms only behind the *large* wave. However, the presence of a less active, and more vertically confined, wake is identifiable for both *small* and *baseline* ISWs

when the color-bar limits are adjusted as shown in the inset figures 11b and 11c respectively, which correspond to the black-outlined box in the larger field-of-view.

Unlike Lien et al. (2014) who suggest that the wake results from convective instability of the ISW, figures 10 & 11a indicate a distinct link of the simulated wake to the shear instabilities and clockwise-rotating K-H billows generated at the wake trough. The *large* wave (sampled here at a later time as compared to fig. 10a) in particular develops a uniquely visible wake in its rear, consisting of interfacial wave-like features whose wavelength is consistent with the spacing of the clockwise-rotating billows generated at the ISW trough (fig. 10a and c). Note, however, that any density overturns *in the wake* of the *large* ISW indicate stirring by a counter-clockwise rotation as they are caused by the subsequent evolution of negative  $y$ -vorticity features produced at the ISW rear shoulder (fig. 10c). Although these counter-clockwise billows are clearly left behind the ISW, determining whether they propagate away from the wave and at what speed would require a higher postprocessing file output rate than the one currently used (section 2e1).

The vertical overturns and turbulent motions linked to billow-breaking suggest additional active mixing of the background stratified water column for long distance at the wake of the ISW ( $O(10km)$ ). Finally, for the case of only the *large* wave, large-scale overturns on the  $y - z$  plane, up to 15m-tall, are observed in the ISW wake (not shown).

Instantaneous potential density profiles sampled in each wave's *wake* (1.14km behind the trough, also shown by the vertical white dashed lines in Fig. 11a) are shown in Fig. 11d. The location of the wake-profile sampling is chosen appropriately aiming to juxtapose the large potential density inversions produced by the *large* wave, especially as compared to the *small* and *baseline* simulated waves. The earlier along-transect sampling location for the *small* is because the particular simulation was stopped at a slightly earlier time (its last output is actually shown in Fig. 11) with respect to the *large* and *baseline* waves.

The profiles at hand show a highly perturbed water column only for the *large* wave (Fig. 11d). The associated deviations from the reference background profile for the *small* and *baseline* ISW are negligible, as these profiles remain almost unperturbed with respect to their initial deep-water structure. However, for the *large* wave, a density inversion larger than  $1 kg/m^3$  between 20 and 30m of depth is observed. Such high deviations are potentially linked with high available potential

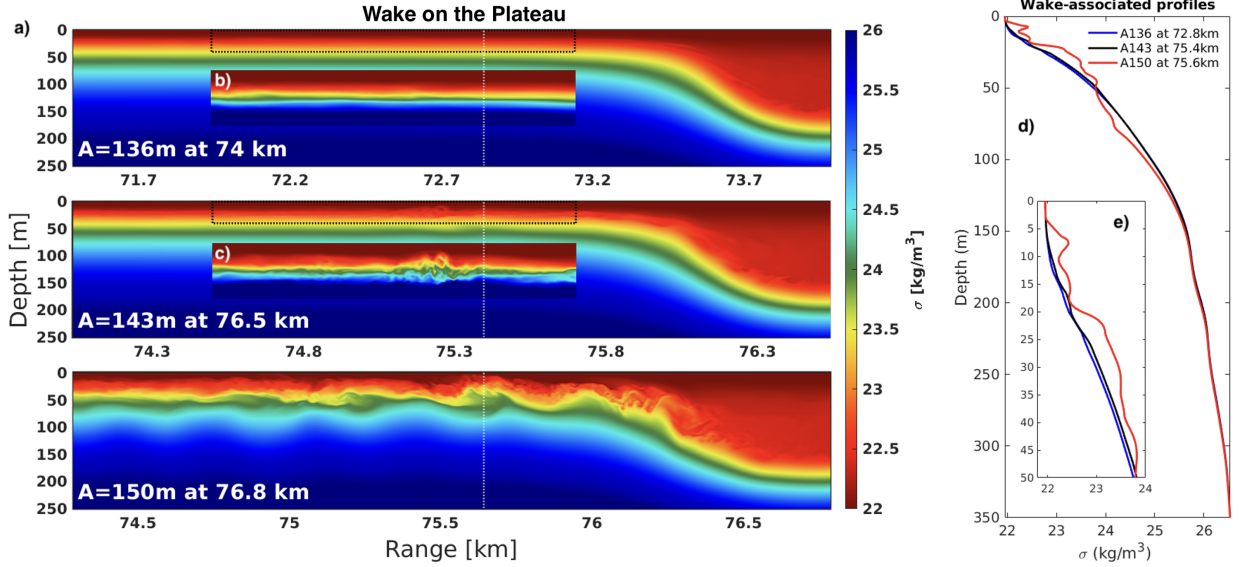


FIG. 11. Midplane potential density contour of the wake produced on the plateau for all three simulated waves (a). Panels (b) and (c) visualize the corresponding black-outlined boxes in (a) with a reduced range in the colorbar limits ( $[22 \ 23] \text{kg/m}^3$ ). The vertical white dotted lines indicate the location of profiles sampled and shown in (d). A zoomed view of the near-surface region (top 50m) is shown in e, emphasizing the large density disturbances for the *large* wave.

energy and continuous turbulent mixing of the water column which would then non-trivially modify the background state of potential energy (Winters et al. 1995).

## 6) KINETIC ENERGY EVOLUTION

The Perturbation Kinetic Energy per unit mass of the fluctuating velocity components, integrated over a finite volume that encompasses the wave, is defined as

$$\mathbf{PKE} = \frac{1}{2} \int_V (u'^2 + v'^2 + w'^2) dV . \quad (5)$$

The quantities denoted in primes represent the fluctuation of each velocity component with respect to its  $y$ -averaged counterpart (denoted with  $\langle y \rangle$ ) obtained from the instantaneous three-dimensional instantaneous field at a given location along the wave propagation track.

Typically the quantity defined in equation (5) would be regarded as ‘‘Turbulent Kinetic Energy’’ (Tennekes and Lumley 1972) as it is representative of the turbulent fluctuations in the flow. This

is indeed the case for the associated fluctuating flow field that develops after the initial convective instability, as shown in figures 4 and 6 per the complex finer-scale structure with appreciable scale separation found in the wave core. As discussed in section 3b 4, the K-H billows produced by shear instability do not become fully turbulent when evolving three-dimensionally, due to insufficient lateral resolution and the use of a spectral filter. Hence, hereafter the term “Perturbation Kinetic Energy” (PKE) will be used.

PKE contours of the Root-Mean-Square average in the transverse direction for all three ISWs are shown using logarithmic color bars for two snapshots of wave evolution (60 and 70 km respectively) in Fig. 12. Although the larger the wave, the broader the along-wave extent of the high PKE region, all simulated waves show qualitatively similar behavior in their evolution (see also supplementary animations). At the *shallow* mooring (60km), the PKE is driven by velocity perturbations due to the convective instability, the associated entrainment of heavier water linked to the plunging isopycnals and the subsequent horizontally propagating gravity current. The PKE distribution is relatively uniform within at least the gravity current as delineated by the black-line isopycnal (that corresponds to the red isopycnal of figures 4 and 6 with the color switch performed to enhance visibility) in Fig. 12. The top right fraction of the ISW interior remains relatively inactive through the entire simulation, when compared to the mid-and-rear part of the wave core.

The PKE values within the more energetic fraction of the interior of each ISW are amplified by almost one order of magnitude on the plateau (70km - right panels of Fig. 12) as compared to the shallow mooring region (60km); the amplification is apparently due to the establishment of shear instabilities. Furthermore, larger PKE values are more localized near the trough and the tail of the wave, consistently with the trajectory of associated K-H billows (Fig. 10), and the corresponding wake, particularly for the case of the *large* ISW.

Figure 13a shows the evolution of the wave-integrated PKE (equation 5) per unit mass as a function of position along the propagation track. The associated integration is performed within a 50m-wide, two-wavelength-long ( $\sim 2km$ ) and 250m-deep box, which is horizontally centered at the ISW trough and encompasses the full wave. Note that the particular integration window does not account for the Kinetic Energy of the K-H-billow-driven wake. A weak initial reduction in PKE amplitude evolution visible for the *small* wave, also observed for the *baseline* wave earlier in the transect (not shown here), is due to the transient adjustment of the inserted perturbations



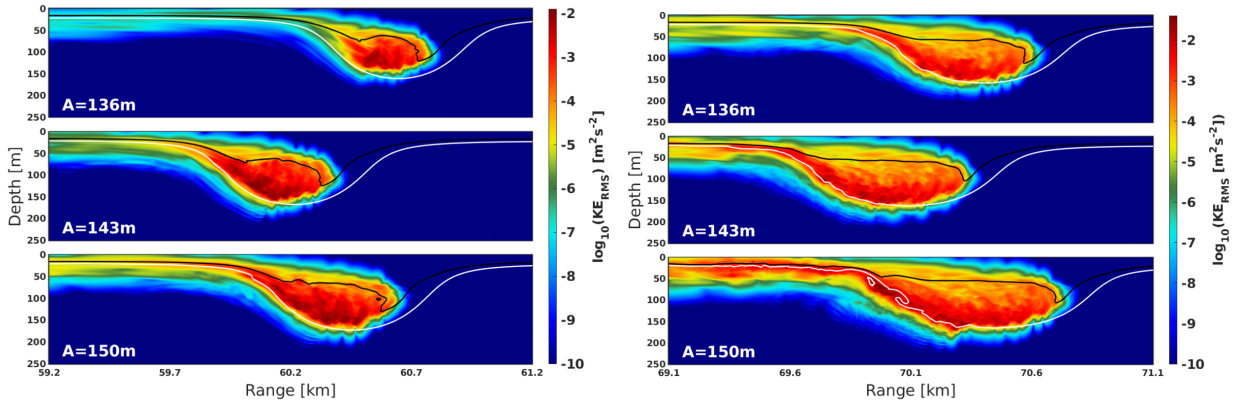


FIG. 12. Contours of Perturbation Kinetic Energy (PKE) at 60 (left) and 70 km (right). Note the logarithmic scale on the color bars, which is not the same between the two locations along the propagation track. The PKE content of the more energetic fraction of each ISW interior is amplified for almost one order of magnitude on the plateau (70km) compared to the *shallow* mooring region (60km). The white and black contour lines correspond to those in red and grey in figures 4 and 6 and are used to delineate the subsurface recirculating core and approximate edge of the gravity current and the ISW waveform, respectively. The full PKE evolution across all cases may be found in the supplementary animation.

(section 2e 1) to correlate with the preexisting ISW-dominated two-dimensional flow field and any reduction of the associated velocity magnitude because of the pressure projection step of the flow solver which ensures the perturbation velocity field is fully incompressible (Olivier Desjardins, pers. comm. and Diamantopoulos et al. (2022)).

For all three ISWs, one subsequently discerns two regimes of PKE evolution along the transect; at any location, PKE magnitude increases with wave amplitude. In each regime, the wave-integrated PKE curve has a linear slope, indicating exponential growth. Between 53 and 60km, steep, vigorous growth of the PKE is observed, apparently driven by the convective instability. The onset of this growth is delayed with decreasing ISW amplitude, consistent with the corresponding delay in instability onset (Fig. 5). The slope of the PKE curve is comparable for all three waves in this first regime, particularly between 57 and 60km. Prior to that point, a slower growth rate is observed for the *large* wave presumably due to the residual perturbations from the weaker, shorter-lived, convective instability event in deeper waters (section 3b 1). Along the remaining part of the transect, including the plateau where shear instabilities dominate, the PKE continues to increase, albeit at a visibly slower rate. Recall that despite this reduced growth rate, the maximum PKE

values are non-trivially larger than their deeper-water counterparts (left vs. right panels of Fig. 12). However, in the latter case, PKE is confined near the pycnocline and does not permeate the bulk of the ISW core.

In Fig. 13b, the contribution of each individual velocity component to PKE evolution is shown strictly for the *large* wave, noting the run's earlier time of transition to three-dimensional mode and perturbation insertion (section 2e 1). The curves are plotted from this time onward. Per the practice of inserting noise in only the  $u$  and  $w$  velocity components, the transverse ( $v$ ) component does rapidly grow from a zero value and eventually becomes comparable in magnitude to the vertical ( $w$ ) component. The three curves distinctly overlap only for a short propagation range ( $\sim 55 - 60$  km) linked with the most intense phase of the convective instability development. On the remaining part of the transect, the along-wave ( $u$ ) component is consistently elevated with respect to the other two components. Such behavior should be expected since the dominant contributor to vertical shear, and turbulence production (Pope 2000), in the along-wave propagation plane originates from the horizontal background and wave-induced current. Qualitatively similar behavior for the remaining two waves (not shown) is also observed.

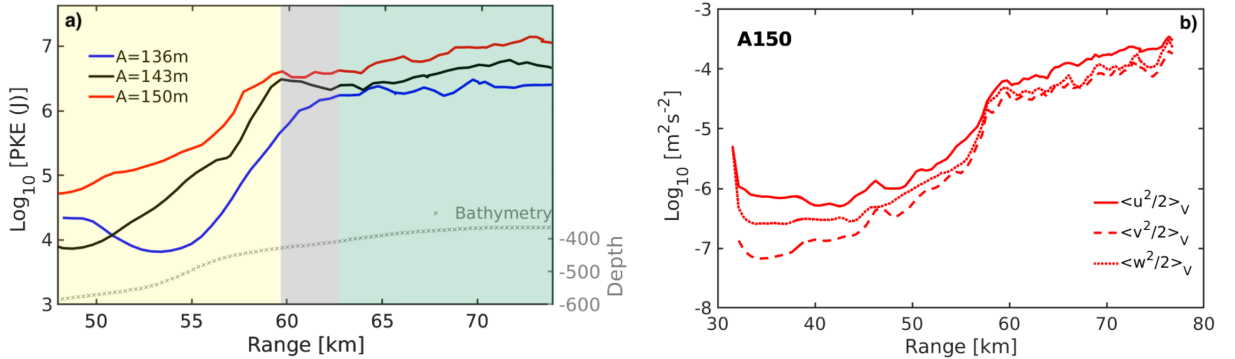


FIG. 13. **a**: Total Perturbation Kinetic Energy per unit mass integrated (equation 5) over a prescribed volume,  $V$ , horizontally centered around the ISW for all three ISWs, and **b**: PKE contribution of each fluctuating velocity component for the *large* wave. Both quantities are shown as a function of the position of the ISW trough along the transect. In panel a), the yellow-shaded area shows the convectively-unstable-dominated regime, while the green one denotes the shear-instability-dominated regime. The gray area represents the transition between the two regimes. The gray symbols on the bottom denote the bathymetry over this region, for reference.

#### 4. Discussion and Concluding Remarks

In this paper, the shoaling of high-amplitude internal solitary waves (ISWs) over a select, near-isobath-normal, transect of the South China Sea has been examined using turbulence-resolving simulations (at spatial and temporal resolutions of  $[0.21m, 1m]$ , across all three spatial directions, and  $0.2s$ , respectively) equipped with realistic profiles of background current and stratification. The use of a state-of-the-art numerical modeling approach (Diamantopoulos et al. 2022) has enabled the reproduction, at such high-resolution over the entire wave propagation track (extending over  $80km$  and spanning depths from  $921m$  to  $365m$ ), of key features of the corresponding in-situ observed phenomenology (Lien et al. 2012, 2014 & Chang et al. 2021a,b). For three simulated ISWs, of varying initial amplitude (corresponding to maximum isopycnal displacements of  $136, 143,$  and  $150m$ ), the evolution of the wave-scale response has been captured in detail along with the development of associated convective and shear instabilities and the larger turbulent scales therein.

The convective instability and the resulting subsurface recirculating core formation occur in a similar fashion across all three waves. However, the onset of convective instability occurs earlier along the transect with increasing initial wave amplitude. The enhanced spatial resolution of the simulations reveals a particular aspect of the convective instability evolution, previously not reported in the field: for all simulated waves, the convective instability leads to the entrainment of heavier water from the rear shoulder of the wave which plunges into the wave interior. Upon sufficient accumulation of heavier water inside the rear of the wave, a gravity current is then initiated which advances to the ISW's leading edge further advecting the heavier water with it. The waveform remains distinctly symmetric throughout this process. Both the convective plunging and gravity current generate turbulence across the entire wave interior which visibly mixes the rear of the ISW but also weakens the stratification at the wave trough. Local patches of Richardson number below  $0.1$  then emerge, giving rise to shear instability and Kelvin-Helmholtz (K-H) billows. Although the amplitude of the three simulated waves varies only by an additive factor of  $7m$ , K-H billow size and their signature behind the wave grow nonlinearly with wave amplitude.  $50m$ -tall billows are observed within the largest simulated wave upon its arrival on the shallower water plateau at  $360m$  depth. A visible and highly energetic wake, persisting  $5km$  behind the wave, is observed in this case as contrasted to the two lower-amplitude ISWs where only weak intermittent bursts of turbulent-like motion occur in the lee of the wave.

The perturbation kinetic energy of the shear-instability-dominated stage is focused along the billow propagation path, i.e., the pycnocline and wake but is at least one order of magnitude larger than that produced by its wave-filling counterpart through the antecedent convective instability. Each of the two instabilities imparts its own near-exponential growth rate in the wave-integrated along-shoaling-track evolution of the perturbation kinetic energy further marking the delineation between two separate evolution regimes in the shoaling ISWs.

The results reported here serve as the springboard for ongoing and future analysis of the existing datasets and future larger-scale high-accuracy/resolution simulations to investigate a number of open questions that have emerged in this manuscript in regard to the turbulence dynamics of shoaling ISWs on the continental slope. Once these remaining open questions are addressed, the ground should be mature for modeling of relevant, and more complex and diverse, ISW-driven processes in shallower waters as recently reported through several recent studies (Colosi et al. 2018; Davis et al. 2020; Ramp et al. 2022a,b; Sinnett et al. 2022; Whitwell et al. 2024).

*Acknowledgments.* The authors are grateful to Professors Marek Stastna, Jim Riley, Steve de Bruyn Kops, Greg Ivey, Larry Armi, and Olivier Desjardins for several insightful conversations on turbulence in breaking internal solitary waves. This work has been primarily supported by the National Science Foundation (NSF) grant OCE-1634257. Additional support by grants NSF-OCE 1948251 and NSF-OCE 1634182 is also acknowledged. This work used Stampede2 at TACC through allocation TG-EES200010 from the Extreme Science and Engineering Discovery Environment (XSEDE), which was supported by National Science Foundation grant number 1548562. Moreover, this work used Stampede2 at TACC through allocation TG-EES200010 from the Advanced Cyberinfrastructure Coordination Ecosystem: Services & Support (ACCESS) program, which is supported by National Science Foundation grants 2138259, 2138286, 2138307, 2137603, and 2138296.

*Data availability statement.* Data used to produce the main analysis and figures contained in this manuscript are available by request. Further details can be found at <https://diamessis.github.io>.

## References

- Aigner, A., D. Broutman, and R. Grimshaw, 1999: Numerical simulations of internal solitary waves with vortex cores. *Fluid Dyn. Res.*, **25** (6), 315, [https://doi.org/10.1016/S0169-5983\(98\)00046-X](https://doi.org/10.1016/S0169-5983(98)00046-X).
- Barad, M., and O. Fringer, 2010: Simulations of shear instabilities in interfacial gravity waves. *J. Fluid Mech.*, **644**, 61 – 95, <https://doi.org/10.1017/S0022112009992035>.
- Boerner, T. J., S. Deems, T. R. Furlani, S. L. Knuth, and J. Towns, 2023: Access: Advancing innovation: NSF’s advanced cyberinfrastructure coordination ecosystem: Services & support. *Practice and Experience in Advanced Research Computing*, Association for Computing Machinery, New York, NY, USA, 173–176, PEARC ’23, <https://doi.org/10.1145/3569951.3597559>.
- Boyd, J. P., 1998: Two comments on filtering (artificial viscosity) for Chebyshev and Legendre spectral and spectral element methods: Preserving boundary conditions and interpretation of the filter as a diffusion. *J. Comput. Phys.*, **143** (1), 283–288, <https://doi.org/https://doi.org/10.1006/jcph.1998.5961>.

- Canuto, C., M. Hussaini, A. Quarteroni, and T. Zang, 2007: *Spectral Methods: Evolution to Complex Geometries and Applications to Fluid Dynamics*. Scientific Computation, Springer Berlin Heidelberg, <https://doi.org/10.1007/978-3-540-30728-0>.
- Carpenter, J., G. Lawrence, and W. Smyth, 2007: Evolution and mixing of asymmetric Holmboe instabilities. *J. Fluid Mech.*, **582**, 103 – 132, <https://doi.org/10.1017/S0022112007005988>.
- Carr, M., J. Franklin, S. E. King, P. A. Davies, J. Grue, and D. G. Dritschel, 2017: The characteristics of billows generated by internal solitary waves. *J. Fluid Mech.*, **812**, 541–577, <https://doi.org/10.1017/jfm.2016.823>.
- Carr, M., D. Fructus, J. Grue, A. Jensen, P. Davies, and S. Dalziel, 2008: Convectively induced shear instability in large amplitude internal solitary waves. *Phys. Fluids*, **20**, <https://doi.org/10.1063/1.3030947>.
- Carr, M., S. King, and D. Dritschel, 2012: Instability in internal solitary waves with trapped cores. *Phys. Fluids*, **24**, <https://doi.org/10.1063/1.3673612>.
- Carr, M., S. E. King, and D. G. Dritschel, 2011: Numerical simulation of shear-induced instabilities in internal solitary waves. *J. Fluid Mech.*, **683**, 263–288, <https://doi.org/10.1017/jfm.2011.261>.
- Carter, G. S., M. C. Gregg, and R.-C. Lien, 2005: Internal waves, solitary-like waves, and mixing on the Monterey Bay shelf. *Cont. Shelf Res.*, **25 (12)**, 1499–1520, <https://doi.org/10.1016/j.csr.2005.04.011>.
- Chang, M.-H., 2021: Marginal instability within internal solitary waves. *Geophys. Res. Lett.*, **48 (9)**, e2021GL092616, <https://doi.org/10.1029/2021GL092616>.
- Chang, M.-H., R.-C. Lien, K. Lamb, and P. Diamessis, 2021a: Long-term observations of shoaling internal solitary waves in the Northern South China Sea. *J. Geophys. Res.: Oceans*, **126**, <https://doi.org/10.1029/2020JC017129>.
- Chang, M.-H., and Coauthors, 2021b: Direct measurements reveal instabilities and turbulence within large amplitude internal solitary waves beneath the ocean. *Commun. Earth Environ.*, **2 (1)**, 15, <https://doi.org/10.1038/s43247-020-00083-6>.

- Cheng, Y.-H., M.-H. Chang, Y. J. Yang, S. Jan, S. R. Ramp, K. A. Davis, and D. B. Reeder, 2024: Insights into internal solitary waves east of Dongsha Atoll from integrating geostationary satellite and mooring observations. *J. Geophys. Res.*, **129** (8), <https://doi.org/10.1029/2024JC021109>.
- Colosi, J. A., N. Kumar, S. H. Suanda, T. M. Freismuth, and J. H. MacMahan, 2018: Statistics of internal tide bores and internal solitary waves observed on the inner continental shelf off Point Sal, California. *J. Phys. Oceanogr.*, **48** (1), 123–143, <https://doi.org/10.1175/JPO-D-17-0045.1>.
- Davis, K. A., R. S. Arthur, E. C. Reid, J. S. Rogers, O. B. Fringer, T. M. DeCarlo, and A. L. Cohen, 2020: Fate of internal waves on a shallow shelf. *J. Geophys. Res.: Oceans*, **125** (5), <https://doi.org/10.1029/2019JC015377>.
- Diamantopoulos, T., 2021: A high-order hybrid flow solver for the simulation of non-linear internal waves in long complex domains: exploring the turbulent aspects of a recirculating core in a shoaling internal solitary wave of depression. <https://doi.org/10.7298/j0ff-3h90>.
- Diamantopoulos, T., S. Joshi, G. Thomsen, G. Rivera-Rosario, P. Diamessis, and K. Rowe, 2022: A high accuracy/resolution spectral element/Fourier-Galerkin method for the simulation of shoaling non-linear internal waves and turbulence in long domains with variable bathymetry. *Ocean Model*, **176**, 102 065, <https://doi.org/10.1016/j.ocemod.2022.102065>.
- Diamessis, P., J. Domaradzki, and J. Hesthaven, 2005: A spectral multidomain penalty method model for the simulation of high Reynolds number localized stratified turbulence. *J. Comput. Phys.*, **202**, 298–322, <https://doi.org/10.1016/j.jcp.2004.07.007>.
- Diamessis, P., and L. Redekopp, 2006: Numerical investigation of solitary internal wave-induced global instability in a shallow water benthic boundary layers. *J. Phys. Oceanogr.*, **36**, 784–812, <https://doi.org/10.1175/JPO2900.1>.
- Duda, T., J. Lynch, J. Irish, R. Beardsley, S. Ramp, C.-S. Chiu, T.-Y. Tang, and Y.-J. Yang, 2004: Internal tide and nonlinear internal wave behavior at the continental slope in the Northern South China Sea. *IEEE J. Oceanic Eng.*, **29** (4), <https://doi.org/10.1109/JOE.2004.836998>.
- Dunphy, M., C. Subich, and M. Stastna, 2011: Spectral methods for internal waves: indistinguishable density profiles and double-humped solitary waves. *Nonlinear Proc. Geoph.*, **18**, 351–358, <https://doi.org/10.5194/npg-18-351-2011>.

- Fringer, O., and R. Street, 2003: The dynamics of breaking progressive interfacial waves. *J. Fluid Mech.*, **494**, 319–353, <https://doi.org/10.1017/S0022112003006189>.
- Fructus, D., M. Carr, J. Grue, A. Jensen, and P. Davies, 2009: Shear-induced breaking of large internal solitary waves. *J. Fluid Mech.*, **18**, 351–358, <https://doi.org/10.1017/S0022112008004898>.
- Gottlieb, D., and J. Hesthaven, 2001: Spectral methods for hyperbolic problems. *J. Comp. Appl. Math.*, **128** (1), 83–131, <https://doi.org/10.1016/bs.hna.2016.09.007>, numerical Analysis 2000. Vol. VII: Partial Differential Equations.
- He, Y., K. Lamb, and R.-C. Lien, 2019: Internal solitary waves with subsurface cores. *J. Fluid Mech.*, **873**, 1–17, <https://doi.org/10.1017/jfm.2019.407>.
- Helfrich, K., 1992: Internal solitary wave breaking and run-up on a uniform slope. *J. Fluid Mech.*, **243**, 133–154, <https://doi.org/10.1017/S0022112092002660>.
- Helfrich, K., and W. Melville, 2006: Long nonlinear internal waves. *Annu. Rev. Fluid Mech.*, **38**, 395–425, <https://doi.org/10.1146/annurev.fluid.38.050304.092129>.
- Huang, S., X. Huang, W. Zhao, Z. Chang, X. Xu, Q. Yang, and J. Tian, 2022: Shear instability in internal solitary waves in the Northern South China Sea induced by multiscale background processes. *J. Phys. Oceanogr.*, **52** (12), 2975 – 2994, <https://doi.org/10.1175/JPO-D-21-0241.1>.
- Jackson, C., J. da Silva, and G. Jeans, 2012: The generation of nonlinear internal waves. *Oceanography*, **25**, <https://doi.org/10.5670/oceanog.2012.46>.
- Jacobitz, F., S. Sarkar, and C. Van Atta, 1997: Direct numerical simulations of the turbulence evolution in a uniformly sheared and stably stratified flow. *J. Fluid Mech.*, **342**, 231–261.
- Joshi, S., G. Thomsen, and P. Diamessis, 2016: Deflation-accelerated preconditioning of the Poisson–Neumann Schur problem on long domains with a high-order discontinuous element-based collocation method. *J. Comput. Phys.*, **313** (209-232), <https://doi.org/https://doi.org/10.1016/j.jcp.2016.02.033>.
- Karniadakis, G., M. Israeli, and S. Orszag, 1991: High-order splitting methods for the incompressible navier-stokes equations. *J. Comput. Phys.*, **97**, 411–443, [https://doi.org/10.1016/0021-9991\(91\)90007-8](https://doi.org/10.1016/0021-9991(91)90007-8).



- Karniadakis, G., and S. Sherwin, 2005: *Spectral/HP Element Methods for Computational Fluid Dynamics*. <https://doi.org/10.1093/acprof:oso/9780198528692.001.0001>.
- Kirby, R., and G. Karniadakis, 2003: De-aliasing on non-uniform grids: Algorithms and applications. *J. Comput. Phys.*, **191**, 249–264, [https://doi.org/10.1016/S0021-9991\(03\)00314-0](https://doi.org/10.1016/S0021-9991(03)00314-0).
- Klymak, J., and J. Moum, 2003: Internal solitary waves of elevation advancing on a shoaling shelf. *Geophys. Res. Lett.*, **30** (20), <https://doi.org/10.1029/2003GL017706>, 2045.
- Koop, G., and G. Butler, 1981: An investigation of internal solitary waves in a two-fluid system. *J. Fluid Mech.*, **112**, 225–251, <https://doi.org/10.1017/S0022112081000372>.
- Lamb, K., 2002: A numerical investigation of solitary internal waves with trapped cores formed via shoaling. *J. Fluid Mech.*, **451**, 109–144, <https://doi.org/10.1017/S002211200100636X>.
- Lamb, K., 2003: Shoaling solitary internal waves: on a criterion for the formation of waves with trapped cores. *J. Fluid Mech.*, **478**, 81–100, <https://doi.org/10.1017/S0022112002003269>.
- Lamb, K., and D. Farmer, 2011: Instabilities in an internal solitary-like wave on the Oregon Shelf. *J. Phys. Oceanogr.*, **41**, 67–87, <https://doi.org/https://doi.org/10.1175/2010JPO4308.1>.
- Lamb, K., and A. Warn-Varnas, 2015: Two-dimensional numerical simulations of shoaling internal solitary waves at the ASIAEX site in the South China Sea. *Nonlinear Proc. Geoph.*, **22**, 289–312, <https://doi.org/https://doi.org/10.5194/npg-22-289-2015>.
- Lamb, K. G., R.-C. Lien, and P. J. Diamessis, 2019: Internal solitary waves and mixing. *Encyclopedia of Ocean Sciences (Third Edition)*, J. K. Cochran, H. J. Bokuniewicz, and P. L. Yager, Eds., third edition ed., Academic Press, Oxford, 533–541, <https://doi.org/https://doi.org/10.1016/B978-0-12-409548-9.10951-0>.
- Lien, R.-C., E. D’Asaro, F. Henyey, M.-H. Chang, T.-Y. Tang, and Y.-J. Yang, 2012: Trapped core formation within a shoaling nonlinear internal wave. *J. Phys. Oceanogr.*, **42**, 511–525, <https://doi.org/10.1175/2011JPO4578.1>.
- Lien, R.-C., F. Henyey, B. Ma, and Y.-J. Yang, 2014: Large-amplitude internal solitary waves observed in the northern South China Sea: Properties and energetics. *J. Phys. Oceanogr.*, **44** (4), 1095–1115, <https://doi.org/10.1175/JPO-D-13-088.1>.

- Lien, R.-C., T. Yang, M. Chang, and E. D'Asaro, 2005: Energy of nonlinear internal waves in the South China Sea. *Geophys. Res. Lett.*, **32 (L05615)**, <https://doi.org/10.1029/2004GL022012>.
- Long, R., 1953: Some aspects of the flow of stratified fluids i. a theoretical investigation. *Tellus*, **8**, 460–471, <https://doi.org/10.1111/j.2153-3490.1955.tb01171.x>.
- Lucas, A. J., and R. Pinkel, 2022: Observations of coherent transverse wakes in shoaling nonlinear internal waves. *J. Phys. Oceanogr.*, **52 (6)**, <https://doi.org/10.1175/JPO-D-21-0059.1>.
- Malm, J., P. Schlatter, P. Fischer, and D. Henningson, 2013: Stabilization of the spectral element method in convection dominated flows by recovery of skew-symmetry. *J. Sci. Comput.*, **57**, <https://doi.org/10.1007/s10915-013-9704-1>.
- Moore, S., and R.-C. Lien, 2007: Pilot whales follow internal solitary waves in the South China Sea. *Mar. Mammal Sci.*, **21 (1)**, 193–196, <https://doi.org/10.1111/j.1748-7692.2006.00086.x>.
- Moum, J., D. Farmer, W. Smyth, L. Armi, and S. Vagle, 2003: Structure and generation of turbulence at interfaces strained by internal solitary waves propagating shoreward over the continental shelf. *J. Phys. Oceanogr.*, **33**, 2093–2112, [https://doi.org/10.1175/1520-0485\(2003\)033<2093:SAGOTA>2.0.CO;2](https://doi.org/10.1175/1520-0485(2003)033<2093:SAGOTA>2.0.CO;2).
- Moum, J. N., D. M. Farmer, E. L. Shroyer, W. D. Smyth, and L. Armi, 2007: Dissipative losses in nonlinear internal waves propagating across the continental shelf. *J. Phys. Oceanogr.*, **37 (7)**, 1989–1995, <https://doi.org/10.1175/JPO3091.1>.
- Olsthoorn, J., A. K. Kaminski, and D. M. Robb, 2023: Dynamics of asymmetric stratified shear instabilities. *Phys. Rev. Fluids*, **8**, 024 501, <https://doi.org/10.1103/PhysRevFluids.8.024501>.
- Passaggia, P.-Y., K. R. Helfrich, and B. L. White, 2018: Optimal transient growth in thin-interface internal solitary waves. *J. Fluid Mech.*, **840**, 342–378, <https://doi.org/10.1017/jfm.2018.19>.
- Pope, S., 2000: *Turbulent Flows*. Cambridge University Press, [https://doi.org/10.1016/S0010-2180\(01\)00244-9](https://doi.org/10.1016/S0010-2180(01)00244-9).
- Ramp, S., Y. Yang, C.-S. Chiu, D. Reeder, and F. Bahr, 2022a: Observations of shoaling internal wave transformation over a gentle slope in the South China Sea. *Nonlinear Proc. Geoph.*, **29**, 279–299, <https://doi.org/10.5194/npg-29-279-2022>.

- Ramp, S. R., and Coauthors, 2022b: Solitary waves impinging on an isolated tropical reef: Arrival patterns and wave transformation under shoaling. *J. Geophys. Res.: Oceans*, **127** (3), <https://doi.org/10.1029/2021JC017781>.
- Rivera-Rosario, G., P. Diamessis, R.-C. Lien, K. Lamb, and G. Thomsen, 2022: Three-dimensional perspective on a convective instability and transition to turbulence in an internal solitary wave of depression shoaling over gentle slopes. *Env. Fluid Mech.*, <https://doi.org/10.1007/s10652-022-09844-7>.
- Rivera-Rosario, G., P. J. Diamessis, R.-C. Lien, K. G. Lamb, and G. N. Thomsen, 2020: Formation of Recirculating Cores in Convectively Breaking Internal Solitary Waves of Depression Shoaling over Gentle Slopes in the South China Sea. *J. Phys. Oceanogr.*, **50** (5), 1137–1157, <https://doi.org/10.1175/JPO-D-19-0036.1>.
- Salehipour, H., C. P. Caulfield, and W. R. Peltier, 2016: Turbulent mixing due to the Holmboe wave instability at high Reynolds number. *J. Fluid Mech.*, **803**, 591–621, <https://doi.org/10.1017/jfm.2016.488>.
- Salehipour, H., W. Peltier, and C. Caulfield, 2018: Self-organized criticality of turbulence in strongly stratified mixing layers. <https://doi.org/10.17863/CAM.33527>.
- Sandstrom, H., and J. Elliott, 1984: Internal tide and solitons on the Scotian shelf: A nutrient pump at work. *J. Geophys. Res.*, **89** (C4), 6415–6426, <https://doi.org/10.1029/JC089iC04p06415>.
- Schmid, P., and D. Henningson, 2001: *Stability and Transition in Shear Flows*, Vol. 142. <https://doi.org/10.1007/978-1-4613-0185-1>.
- Scotti, A., and J. Pineda, 2004: Observation of very large and steep internal waves of elevation near the massachusetts coast. *Geophys. Res. Lett.*, **31** (22), <https://doi.org/10.1029/2004GL021052>, 122307.
- Shroyer, E., J. Moum, and J. Nash, 2011: Nonlinear internal waves over New Jersey’s continental shelf. *J. Geophys. Res.*, **116** (C03022), <https://doi.org/10.1029/2010JC006332>.
- Sinnett, G., S. R. Ramp, Y. J. Yang, M.-H. Chang, S. Jan, and K. A. Davis, 2022: Large-amplitude internal wave transformation into shallow water. *J. Phys. Oceanogr.*, **52** (10), 2539 – 2554, <https://doi.org/10.1175/JPO-D-21-0273.1>.

- Smyth, W., and J. Moum, 2000: Length scales of turbulence in stably stratified mixing layers. *Phys. Fluids*, **12** (6), 1327–1342.
- Smyth, W. D., 2004: Kelvin–helmholtz billow evolution from a localized source. *Q. J. Roy. Meteorol. Soc.*, **130** (603), 2753–2766, <https://doi.org/https://doi.org/10.1256/qj.03.226>.
- Smyth, W. D., and J. R. Carpenter, 2019: *Instability in Geophysical Flows*. Cambridge University Press, <https://doi.org/10.1017/9781108640084>.
- Stastna, M., 2022: *Internal Waves in the Ocean: Theory and Practice*. Springer Cham, <https://doi.org/10.1007/978-3-030-99210-1>.
- Stastna, M., and K. Lamb, 2002: Large fully nonlinear internal solitary waves: The effect of background current. *Phys. Fluids*, **14** (9), 2987–2999, <https://doi.org/10.1063/1.1496510>.
- Stastna, M., and K. Lamb, 2008: Sediment resuspension mechanism associated with internal waves in coastal waters. *J. Geophys. Res.*, **113**, <https://doi.org/10.1146/annurev-fluid-122316-045049>.
- Stastna, M., and S. Legare, 2024: Simulations of shoaling large-amplitude internal waves: perspectives and outlook. *Flow*, **4**, <https://doi.org/10.1017/flo.2024.9>.
- Tennekes, H., and J. Lumley, 1972: *A First Course in Turbulence*. MIT Press, <https://doi.org/10.1017/S002211207321251X>.
- Thyng, K., C. Greene, R. Hetland, H. Zimmerle, and S. Dimarco, 2016: True colors of oceanography: Guidelines for effective and accurate colormap selection. *Oceanography*, **29**, 9–13, <https://doi.org/10.5670/oceanog.2016.66>.
- Towns, J., and Coauthors, 2014: Xsede: Accelerating scientific discovery. *Computing in Science & Engineering*, **16** (5), 62–74, <https://doi.org/10.1109/MCSE.2014.80>.
- Troy, C., and J. Koseff, 2005: The instability and breaking of long internal waves. *J. Fluid Mech.*, **543**, 107–136, <https://doi.org/10.1017/S0022112005006798>.
- Turkington, B., A. Eydeland, and S. Wang, 1991: A computational method for solitary internal waves in a continuously stratified fluid. *Stud. Appl. Math.*, **85**, 93–127, <https://doi.org/10.1002/sapm199185293>.

- Vlasenko, V., L. Ostrovsky, and K. Hutter, 2005: Adiabatic behavior of strongly nonlinear internal solitary waves in slope-shelf areas. *J. Geophys. Res.*, **110** (C04006), <https://doi.org/10.1029/2004JC002705>.
- Vlasenko, V., N. Stashchuck, and K. Hutter, 2006: Review of baroclinic tides: Theoretical modeling and observational evidence. *Baroclinic Tides*, pp. 372. ISBN 0521843952. Cambridge, UK: Cambridge University Press, July 2005., <https://doi.org/10.1017/CBO9780511535932>.
- Whitwell, C. A., N. L. Jones, G. N. Ivey, M. G. Rosevear, and M. D. Rayson, 2024: Ocean mixing in a shelf sea driven by energetic internal waves. *J. Geophys. Res.: Oceans*, **129** (2), e2023JC019704, <https://doi.org/10.1029/2023JC019704>, e2023JC019704 2023JC019704.
- Winters, K., and E. D'Asaro, 1994: Three-dimensional wave instability near a critical layer. *J. Fluid Mech.*, **272**, 255–284, <https://doi.org/10.1017/S0022112094004465>.
- Winters, K., P. Lombard, J. Riley, and E. D'Asaro, 1995: Available potential energy and mixing in density-stratified fluids. *J. Fluid Mech.*, **289**, 115–128, <https://doi.org/10.1017/S002211209500125X>.
- Winters, K. B., and J. J. Riley, 1992: Instability of internal waves near a critical level. *Dyn. Atmos. Oceans*, **16**, 249–278, [https://doi.org/10.1016/0377-0265\(92\)90009-I](https://doi.org/10.1016/0377-0265(92)90009-I).
- Xu, C., M. Stastna, and D. Deepwell, 2019: Spontaneous instability in internal solitary-like waves. *Phys. Rev. Fluids*, **4**, 014805, <https://doi.org/10.1103/PhysRevFluids.4.014805>.
- Zhang, S., and M. Alford, 2015: Instabilities in nonlinear internal waves on the Washington continental shelf. *J. Geophys. Res.*, **120**, 5272–5283, <https://doi.org/10.1002/2014JC010638>.